



Magnesium-based composites reinforced with graphene nanoplatelets as biodegradable implant materials

Mohammad Shahin , Khurram Munir , Cuie Wen , Yuncang Li *

School of Engineering, RMIT University, Melbourne, Victoria, 3001, Australia



ARTICLE INFO

Article history:

Received 7 January 2020
Received in revised form
20 February 2020
Accepted 21 February 2020
Available online 22 February 2020

Keywords:

Biocorrosion
Graphene
Magnesium metal matrix composite
Strengthening mechanism

ABSTRACT

Magnesium (Mg) and its alloys are considered promising biodegradable implant materials because of their strength and ability to degrade naturally in the body. However, pure Mg degrades rapidly in the physiological environment which adversely affects its mechanical integrity before sufficient bone healing. In this study, a high energy ball mill was used to disperse 0.5 wt% zirconium (Zr) and 0.1 wt% GNPs in Mg powders. Ball milled powder mixtures were then cold pressed under 760 MPa into green compacts and sintered in an argon atmosphere at 610 °C for 2 h. Results indicated that the addition of Zr and GNPs to the Mg matrix significantly enhanced its compressive yield strength by 91% and reduced the corrosion rate by 48% and 68% in electrochemical polarization test and hydrogen evolution test, respectively, compared to pure Mg. The contributions of various strengthening mechanisms to the compressive yield strength of MMNCs were quantitatively predicted in conjunction with validation via experimental results. This study demonstrates the potential of GNPs as effective reinforcement in fabrication of MMNCs with improved mechanical and corrosion properties.

© 2020 Elsevier B.V. All rights reserved.

1. Introduction

The clinical success of biodegradable implants such as bone plates, screws, pins, etc., relies on their natural degradation in the physiological environment without compromising their mechanical integrity before sufficient bone healing [1,2]. In bone-tissue engineering, bone repair and regeneration are promoted by mechanical loading. However, existing implant materials such as stainless steels (SS), cobalt-chromium alloys, and titanium alloys exhibit higher elastic moduli than that of natural bone. This mismatch in elastic modulus between the metallic implant and bone triggers stress-shielding in the host bone tissue which leads to bone resorption and implant loosening, thus requiring additional complicated revision surgery [3].

Magnesium (Mg) and its alloys have emerged as promising candidate materials in recent years for applications in bone-tissue engineering due to their ability to naturally degrade in the body, which eliminates the requirement of revision surgeries. Furthermore, the tensile strength (135–285 MPa), elastic modulus (40–45 GPa), and elongation (2–10%) of pure Mg [3,4] are closer to

those of cortical bone (96–200 MPa, 5.6–14 GPa, and 2%, respectively [5,6]) than other conventional metallic biomaterials. The elastic moduli of the conventional metal implants such as cobalt-chromium alloys (210–240 GPa), stainless steels (190–200 GPa) and titanium alloys (60–110 GPa) [7] are much higher than that of cortical bone. This may cause stress shielding to the surrounding bone, leading to bone resorption and loosening of the implant [8]. However, pure Mg exhibits inadequate mechanical and corrosion properties, which impedes its application in load-bearing implants [9]. For this reason, Mg is generally alloyed with other elements such as aluminum (Al), zinc (Zn), zirconium (Zr), and rare earth elements (REE) to improve its mechanical properties and corrosion resistance.

However, conventional Mg alloys are not necessarily biocompatible because they usually contain toxic alloying elements such as Al. Furthermore, Al-containing Mg alloys such as AZ91 (Mg–9Al–1Zn), AZ61 (Mg–6Al–1Zn), AZ31 (Mg–3Al–1Zn), and AJ62 (Mg–6Al–2Sr) exhibit pitting and stress corrosion in the physiological environment by forming galvanic couples in Mg matrices [10–15]. In addition, an excess amount (≥ 6.0 wt%) of Zn in Mg alloys causes embrittlement, which reduces the mechanical integrity of Mg alloys [16–18]. The surface properties of the implant materials modulate the biological response at the interface of the implant and tissue, leading to bone growth along with the implant

* Corresponding author.

E-mail address: yuncang.li@rmit.edu.au (Y. Li).

material. However, surface damage was observed in a commercial WE43 (Mg-3.5Y-2.3Nd-0.5Zr) Mg alloy due to an uneven pitting effect, leading to a high degradation rate [19,20]. These issues open avenues for further investigation of the potential of various reinforcement materials which can improve the mechanical and corrosion properties of Mg matrices.

Magnesium-based metal matrix nanocomposites (MMNCs) are generally reinforced with bioceramic particles that enhance their mechanical and biological properties, thus providing suitable biodegradable implant materials [21–23]. For example, the addition of alumina (Al_2O_3) nanoparticles enhanced the yield strength of an AZ31B alloy via the Orowan looping effect [24] due to the precipitation of reinforcing particles. Also, MMNCs containing Al_2O_3 , zirconia (ZrO_2), calcium phosphate $\text{Ca}_3(\text{PO}_4)_2$, and yttria (Y_2O_3) reinforcing particles showed promising reinforcing potential in enhancing the mechanical properties of Mg matrices [25]. It was reported that the addition of beta-tricalcium phosphate (β -TCP) reduced the corrosion rate of MMNCs by altering their microstructure (grain refinement) and trigger the formation of a passive film comprised of β -TCP particles on the surface exposed to the physiological environment [26,27]. The grain refinement in metallic materials enables their surfaces to passivate more readily by breaking down the second phase intermetallic particles along the grain boundaries which subsequently enhances their corrosion resistance [28–30]. Similarly, Mg matrix reinforced with silicon nitride (Si_3N_4) showed cytocompatibility with MG-63, L929, and human mesenchymal stem cells (HMSC) and also stimulated new bone growth [31,32]. The addition of hydroxyapatite (HA) and fluorapatite (FA) particles reduced the porosity of Mg-based composites, leading to enhanced corrosion resistance in artificial seawater and viability of MG63 cell lines [33,34].

Similarly, it was reported that graphene nanoplatelets (GNPs) enhanced the mechanical properties of metal matrices via various strengthening mechanisms and also exhibited biocompatibility in contact with blood [35]. Grain refinement of Mg metal matrices by the addition of GNPs is beneficial in enhancing their yield strength and corrosion resistance. The reduction in grain size of MMNCs by addition of GNPs may be attributable to superior thermal conductivity ($5300 \text{ W m}^{-1} \text{ K}^{-1}$) [36] and low coefficient of thermal expansion ($1 \times 10^{-6} \text{ K}^{-1}$) [37] of GNPs compared to Mg ($160 \text{ W m}^{-1} \text{ K}^{-1}$ and $2.61 \times 10^{-5} \text{ K}^{-1}$, respectively). Dispersion of thermally stable GNPs in the Mg matrices forms a network along the grain boundaries due to their lower solubility in Mg, providing pinning effect along the grain boundaries by prohibiting the grain growth [38]. In this context, uniformly dispersed GNPs in pure Mg matrices offer an immense potential to improve its mechanical and corrosion properties [28]. Chen et al. [39] reported that the addition of GNPs enhanced the hardness of Mg matrices. Similarly, Rashad et al. [40–46] reported significant increase in the yield strength, hardness, and elastic modulus of Mg–10Ti–0.18GNPs, Mg–0.3GNPs, Mg–1Al–1Sn–0.18GNPs, Mg–1Al–0.6 GNPs, Mg–1Al–0.09 GNPs, Mg–1Al–0.18GNPs, Mg–1Al–0.3GNPs, AZ61–3GNPs, AZ31–3GNPs, and AZ31–1.5GNPs composites by addition of low concentrations (0.09–3 wt%) of GNPs. However, in these studies, the corrosion behavior of GNP-reinforced pure Mg matrices was not investigated.

In another study, Rashad et al. [46] investigated the electrochemical corrosion behavior of GNP-reinforced AZ series Mg alloys (which contained about 1–10 wt% Al, with Zn content lower than Al) such as AZ31–1.5 wt% GNP, AZ31–3.0 wt% GNP, and AZ61–3.0 wt% GNP in 3.5% sodium chloride solution. The GNP-reinforced AZ series Mg alloys exhibited higher corrosion currents (μA) than those of the AZ31 and AZ61 base alloys. The high corrosion currents in these MMNCs were attributed to a galvanic effect; however, the influence of GNPs on the corrosion behavior of such Mg alloys is still not well-understood. Poor dispersion of GNPs in

the matrix and bimodal grain boundaries might be the reasons for galvanic corrosion in these MMNCs because they were fabricated by casting, in which it is difficult to achieve uniform dispersion of nanoparticles in metal matrices [47]. It has been established that bimodal grain distribution in composites promotes galvanic corrosion [48].

Conversely, the potential of GNPs to act as a corrosion barrier has been widely reported in other studies [49,50]. GNPs possess a unique sp^2 -carbon (C) atomic array forming a two-dimensional honeycomb lattice structure with high electron density, leading to impermeability to all gas molecules. This potential of GNPs is beneficial in preventing rapid corrosion of Mg alloys, since Mg corrosion in physiological environment produces large amount of hydrogen (H_2) gas [51,52]. The large surface area ($2630 \text{ m}^2 \text{ g}^{-1}$) and thin impermeable membrane of GNPs can act as a protective layer on metal matrices, resulting in a reduction in current density and reaction rate during anodic and cathodic scans of GNP-reinforced composites [50,53].

Natural oxidative degradation of GNPs in the physiological environment may occur via enzymatic oxidation by peroxidase [54]. In addition, the strong interaction of both the top and bottom surfaces of GNPs with biomolecules and the wrinkled surface texture of GNPs can promote the binding of biomolecules on their surfaces, enhancing their ability to interlock with the adjacent environment [3,55]. Good binding between the proteins in biological fluids and tissues and GNPs can promote the formation of biocorona proteins on their surfaces [56]. The structure of these biocorona proteins is related to the intrinsic properties of GNPs which make them capable of inducing alteration in the extracellular matrix (ECM), leading to improved biocompatibility in the physiological environment [52,57].

The enzymatic degradation of GNPs by immune-competent cells can accelerate the biocorona interactions inside the body. It was reported that nanocomposites using GNPs electrically stimulated tissues due to their outstanding conductive properties, leading to the acceleration of new bone formation and osteogenic differentiation by adsorbing the ECM proteins [58,59]. Girase et al. [57] also reported π - π stacking and van der Waals (electrostatic) interaction between potential sp^2 -C atoms and biomolecule rings, which led to good adhesion of GNPs to the biomolecules. In addition, remarkable adsorption of bone myogenic protein and morphogenetic protein onto the surface of GNPs enhanced cell adhesion and proliferation [60,61]. Furthermore, nanoflakes of GNPs on implant surfaces can kill bacteria, thus preventing infection during implant surgery [62]. However, a high concentration (1–10 wt%) of GNPs promoted an increase in the stiffness of MMNCs which may not be biomechanically compatible with natural bone [3]. Ultra-high surface area ($2630 \text{ m}^2/\text{g}$) of GNPs impedes their dispersion in metal matrices due to van der Waal (vdW) interactions between individual layers in GNPs. Due to this reason, higher concentrations ($>0.1 \text{ wt}\%$) of GNPs lead to their stacking and agglomeration in the metal matrices. Munir et al. [63] reported the agglomeration of ($>0.1 \text{ wt}\%$) GNPs in Mg matrices which resulted in higher structural defects in their characteristic sp^2 graphitic structure which occur due to friction and impact by neighboring GNPs in a cluster. Moreover, agglomeration of GNPs in Mg matrices adversely affects the mechanical properties of Mg matrices [64] and may trigger micro-galvanic corrosion by becoming cathodic sites in a corrosive environment [63]. Whereas, the safe limit of GNP concentration in biomedical applications was reported to be $50 \mu\text{g}/\text{ml}$ [52].

Therefore, further studies of GNP-reinforced Mg alloys are required in order to better understand the influence of GNP addition on the mechanical and corrosion behavior of Mg-based matrices.

Zr is generally added as an alloying element in Mg alloys for the purpose of grain refinement [65]; however, its high concentration (>5%) forms unalloyed Zr phases in Mg matrices, which adversely affects the corrosion behavior of Mg alloys. The maximum solubility of Zr in Mg alloys was reported as 2.69 wt% [29,66]. Zr and its oxides enhance biocompatibility, blood compatibility, corrosion resistance, cell adhesion and proliferation, and the ability of Mg alloys to reduce adherent bacteria on implant materials [67,68].

In this study, low concentrations of Zr (0.5 wt%) as the alloying element and GNPs (0.1 wt%) as the reinforcing material were added to Mg matrices. The effects of Zr and GNP addition on the mechanical and corrosion properties of the MMNCs were comparatively investigated along with the underlying strengthening mechanisms.

2. Materials and methods

2.1. Starting materials

Pure Mg powder (100 μm particle size, 99.9% purity), Zr powder (40 μm particle size, 99.5% purity), and GNPs (15 μm particle size, 5 nm thickness) (Sigma-Aldrich, Australia) were used as the starting materials. Stearic acid (SA, $\text{C}_{18}\text{H}_{36}\text{O}_2$, purity $\geq 99.9\%$) (Sigma-Aldrich, Australia) was used as the process control agent (PCA) in this study.

2.2. Synthesis of GNP-reinforced MMNC

The GNPs and Zr powder were uniformly dispersed in the Mg powder via high-energy ball-milling (HEBM) using a planetary ball mill (QM 3SP2, China). Stainless steel (SS) balls were used as the milling media and the ball-to-powder ratio (BPR) was maintained at 20:1. SS milling balls of different diameters (7, 10, and 15 mm) were used in order to achieve higher collision energy due to the interference between balls of different diameters which promotes fracturing of the Mg particles over cold welding [38]. Fig. 1 shows a schematic illustration of the processing steps carried out to fabricate the pure Mg, Mg-0.5Zr alloy, and MMNC (Mg-0.5Zr-0.1GNPs) samples. Firstly, Mg powders were ball-milled with 0.5 wt% SA, which was used as the PCA to establish a balance between fracturing and cold-welding of the charged powders during the HEBM process [69]. SS balls according to the BPR were added to the SS vials and high-purity argon (Ar) gas was purged into the milling vials to eliminate any residual oxygen. An interval of 30 min was used between every 30 min of ball-milling to avoid overheating of the charged powders [70]. The ball-milled powders from this batch were used to fabricate the pure Mg sample.

Secondly, 0.5 wt% Zr powders were added to the ball-milled Mg

powders, then further milled for 2 h under the similar milling conditions. This batch of powder mixtures was used to fabricate the Mg-0.5Zr sample. Finally, 0.1 wt% GNPs were added into the previously ball-milled Mg-0.5Zr powder mixture and further milled for 2 h. Pure Mg powder was milled with SA for an optimum duration of 9 h to reduce their particle sizes in the range of 20–40 μm and to attach SA on the surfaces of fractured Mg particles. Whereas, shorter milling durations (≤ 2 h) were used to disperse Zr and GNP particles in Mg powders to avoid phase transformations in Mg–Zr powder mixtures and to avoid severe structural defects in GNPs during their dispersion in Mg–Zr powders [63]. This powder mixture was used to fabricate the MMNC sample. Green compacts with dimensions of 16 mm in diameter and 18 mm in height were prepared by cold-pressing from the as-milled powders at 760 MPa for 30 min using SS dies. The green compacts were firstly sintered at 400 $^{\circ}\text{C}$ for 1 h to remove the PCA and then at 610 $^{\circ}\text{C}$ for 2 h in a furnace purged with high-purity Ar gas.

2.3. Characterization of powder mixtures and consolidated compacts

Different phases and structural changes in the as-received powders, ball-milled powder mixtures, and sintered composites were determined using an X-ray diffractometer (XRD, BrukerAXS D4 Endeavor). All the powder mixtures and sintered composites were scanned over the 2θ angular range of 10–90 $^{\circ}$ using Cu–K radiation ($\lambda = 0.154$ nm) at a scanning rate of 0.02 $^{\circ}$ /sec.

Scanning electron microscopy (SEM) coupled with energy-dispersive X-ray spectrometry (EDX) (FEI Nova NanoSEM) and transmission electron microscopy (TEM, JOEL 1010) were used to analyze the particle size and morphology of the as-received powders and ball-milled powder mixtures, and the dispersion of the GNPs in the Mg matrices and sintered MMNC. For microstructural analysis, disc samples with dimensions of 10 mm in diameter and 2 mm in thickness were machined from the sintered composites by electrical-discharge machining (EDM). The discs were progressively ground using 800, 1200, 2400, and 4000 grit silicon carbide (SiC) grinding papers, followed by mechanical polishing using 0.05 μm colloidal silica-based oxide polishing suspension (OPS) and ethanol in a 50:50 volumetric ratio. After polishing, the disc samples were ultrasonically cleaned in an ethanol solvent and etched using a picral reagent (a solution of 3 ml picric acid, 50 ml ethanol, 5 ml acetic acid, and 10 ml distilled water). Optical microscopy (OM) (Leica DM2500 M with 3.1 MP CCD) was used to analyze the grain structure of the sintered samples. The grain size of the samples was determined using the line intercept method according to ASTM E112-12. The relative densities of the sintered samples were

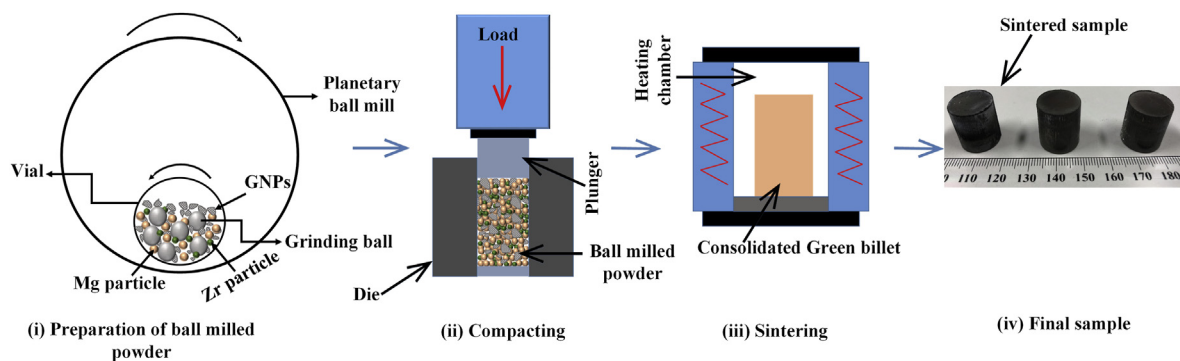


Fig. 1. Processing steps for fabrication of MMNCs.

measured by Archimedes' principle according to standard ASTM <http://www.astm.org/Standards/B962-15>.

2.4. Mechanical property testing

For compression tests, cylindrical samples of 5 mm in diameter and 10 mm in length were machined using EDM according to ASTM E9-09. Compression tests on the sintered composite samples were carried out at room temperature using an uni-axial 50 kN Instron servo-hydraulic testing machine at a constant displacement rate of 0.5 mm/min. Five samples from each group of composite materials were tested to report an average value.

The elastic modulus and nanohardness of the sintered samples were tested using a Hysitron TI-950 TriboIndenter with a Berkovich diamond tip. A maximum load of 10,000 μN and dwell time of 10 s were used during the nanoindentation tests. The indentation was performed in the pattern of a 3×3 array in three different positions on each sample. Indents were separated by 20 μm to avoid the residual stress generated from other indents. The Oliver–Pharr method [71] was used to determine the elastic modulus of the sintered samples. Vickers hardness testing was carried out using a microhardness testing machine (Buehler Omnimet MHT 5104) under a 0.3 Kgf applied load with a 250 μm inter-indentation distance to prevent any residual stress according to ASTM E384 [72]. At least 10 indents were made in each sintered sample and the average values were reported.

2.5. Corrosion property testing

The corrosion properties of the sintered samples were evaluated using three different techniques: (i) electrochemical tests; (ii) hydrogen evolution tests; and (iii) weight-loss tests. Disc samples of 10 mm in diameter and 3 mm in thickness were machined by EDM from the sintered samples for the assessment of corrosion properties. For electrochemical testing, all samples were connected to a copper wire using conductive silver paste and then encapsulated in cold epoxy resin, while the other flat side of the sample with an exposed area of 0.785 cm^2 was ground using SiC grinding paper up to 800 grit followed by degreasing with ethanol and acetone, then ultrasonically cleaned in an ethanol solvent and finally dried in a stream of hot air.

The electrochemical corrosion tests of the mounted samples were carried out in Hanks' Balanced Salt Solution (HBSS) (Sigma-Aldrich, Australia) at 37 °C [73]. A three-electrode cell system with a saturated calomel electrode (SCE) as the reference electrode, a platinum electrode ($1.5 \times 1.5 \text{ cm}^2$) as the counter electrode, and the cold-mounted samples as the working electrode were used. The potentiodynamic polarization curves were measured using a multichannel potentiostat (VSP-300 multi, BioLogic science instrument, France) and the potential was recorded for every 10 mV ranging from -2 V to 1 V. The corrosion current (μA) and the corresponding corrosion rate (CR) (mm y^{-1}) were calculated by the Tafel extrapolation method using EC-Lab software based on ASTM G-102.

For the H_2 evolution tests, the epoxy-mounted samples were placed in HBSS at 37 °C with their exposed surfaces facing upwards. A funnel and burette apparatus was used to cover the samples and collect the released H_2 gas in accordance with the procedures reported in Ref. [74]. Finally, the CR_{H_2} of the pure Mg, Mg-0.5Zr, and MMNC was calculated using the equation given by Ref. [75]:

$$\text{CR}_{\text{H}_2} = 2.27 \times V_{\text{H}_2} \left(\text{mm y}^{-1} \right) \quad (1)$$

where V_{H_2} is the volume ($\text{ml. cm}^{-2} \cdot \text{day}^{-1}$) of the H_2 gas that evolved during dissolution in HBSS.

In the weight-loss tests, the weight (g) of the epoxy-mounted samples was measured using a weight-measuring analytical balance. The surfaces of the samples were exposed in HBSS for 24 h facing upwards and the solution temperature was maintained at 37 °C using a hot plate. After immersion for 24 h, the samples were taken out of the test solution. Preliminary weight loss measurements in corroded samples were recorded using the method described in Ref. [76]. In brief, corroded surfaces were ultrasonically cleaned in ethanol solvent for 300 s and dried in hot air before the weight loss measurements. The CR_{WL} of the pure Mg, Mg-0.5Zr, and MMNC was then calculated using the equation given by Ref. [75]:

$$\text{CR}_{\text{WL}} = 2.1 \times W_L \left(\text{mm y}^{-1} \right) \quad (2)$$

where W_L is the weight-loss rate ($\text{mg. cm}^{-2} \cdot \text{day}^{-1}$) of the sample.

During all the corrosion tests, the ratio of surface area (cm^2) to volume (ml) of HBSS was at 1:300.

3. Results and discussion

3.1. Morphology of as-received powders and ball-milled powder mixtures

Fig. 2 shows the morphologies and corresponding EDX spectra of the as-received Mg, Zr, and GNP powders. The Mg and Zr powders exhibited an irregular flake-like morphology, as shown in Fig. 2a and b. The as-received graphene powders also showed a flake-like morphology with an average particle size of 15 μm (Fig. 2c and d). Fig. 2d shows a TEM image of an individual flaky GNP with a few wrinkled edges. The inset of Fig. 2d shows a selected area electron diffraction (SAED) pattern of the individual GNP. The morphologies of the ball-milled pure Mg, Mg-0.5Zr, and Mg-0.5Zr-0.1GNPs are shown in Fig. 3. The EDX point analysis of the SEM images of the Mg-0.5Zr (Fig. 3b) and Mg-0.5Zr-0.1GNPs (Fig. 3c) powder samples revealed the peaks associated with Zr, carbon (C) and oxygen (O_2), respectively, confirming the dispersion of Zr and GNPs in the Mg powders.

The Feret diameters (d_F) [77] of at least 300 particles were measured from SEM images to calculate the mean particle size of the ball-milled powder mixtures and the results are shown in Fig. 4. The mean particle sizes of the ball-milled Mg-0.5Zr and Mg-0.5Zr-0.1GNPs powder mixtures were 21 μm and 26 μm , respectively, lower than that of the ball-milled pure Mg powder (37 μm). This may be attributable to the dispersion of Zr particles in the Mg matrix, promoting the fracturing of pure Mg particles by shear and impact during the HEBM process.

3.2. XRD diffraction and Raman analysis of powder mixtures and sintered samples

Fig. 5a shows the XRD patterns of the starting materials, ball-milled powder mixtures, and sintered pure Mg, Mg-0.5Zr, and MMNC samples. The XRD pattern obtained from the GNP powder revealed a diffraction peak (002) at $2\theta = 26.5^\circ$ showing the crystalline structure of the as-received GNPs. The XRD pattern obtained from the MMNC sample did not reveal any carbon peaks. This might be due to the lower weight fraction (0.1%) of GNPs in the MMNC powder mixture. Moreover, the X-ray beam loses its intensity by two processes: absorption and scattering. The X-ray mass attenuation coefficient is dependent upon those two processes, which characterizes the flow of penetration of the X-ray beam in the material [78]. The mass attenuation coefficient is different in different $K\alpha$ energy (keV) radiations of an element. Hence, the reason of the absence of C in the XRD pattern of MMNC may be

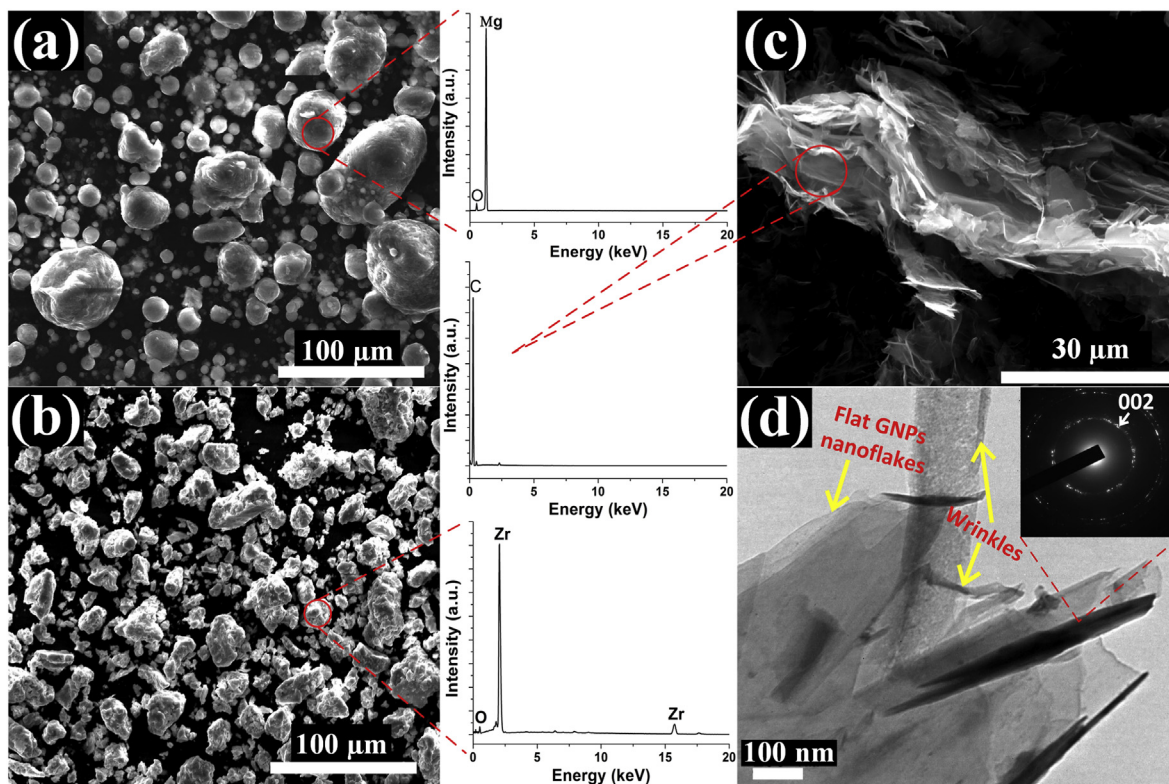


Fig. 2. Morphologies of as-received pure Mg, Zr, and GNP powders: (a) SEM image of pure Mg; (b) SEM image of Zr; (c) SEM image of an individual GNP; and (d) TEM image of an individual GNP with inset showing SAED pattern (red circles indicate EDX mapping area). (For interpretation of the references to colour in this figure legend, the reader is referred to the Web version of this article.)

attributable to the significant difference in the X-ray mass attenuation coefficient of Mg and C which are 4.5×10^2 and $1.3 \times 10^3 \text{ cm}^2 \text{ g}^{-1}$, respectively, at the X-ray $K\alpha$ radiation of Mg (1.254 keV) [38,79] and its low concentration (0.1 wt%) in Mg matrices. There was no evidence of the in situ formation of Mg carbide or Zr carbide phases in the MMNC, indicating the chemical stability of GNPs at an elevated sintering temperature of 610 °C.

Raman spectra of raw GNPs, ball-milled Mg-0.5Zr-0.1GNPs powder, and sintered MMNC are shown in Fig. 5b and the corresponding data are listed in Table 1. Raman spectra obtained from the as-received GNPs (Fig. 5b) revealed three main peaks at 1343, 1575, and 2700 cm^{-1} , which are associated with the characteristic D band, G band and 2D band (or \hat{G} band), respectively [38,63]. The characteristic intensity ratio (I_D/I_G) of D band to G band is an indicator of defect accumulation or structural integrity of dispersed GNP in metal matrices [63]. The I_D/I_G ratio of pristine GNP was measured as 0.54 which increased to 0.81 in the ball milled Mg-Zr-GNP powder mixtures indicating accumulation of non sp^2 defects in the graphitic structure of GNPs during the dispersion processing. These non- sp^2 defects in graphitic structure of carbon nano-materials are usually present in the form of broken edges and vacancies [38]. The I_D/I_G ratio of GNPs in MMNC was measured as 0.21, indicating graphitization-induced healing of GNPs during the high temperature sintering which may occur due to rearrangement and filling of vacancies in their graphitic structure [69]. In addition, Mg atoms can also fill the pores in the structure of GNPs penetrating into the carbon layers during the sintering process, resulting in lower I_D/I_G value compared to the raw GNPs and ball-milled composite powder. Whereas, a ratio between intensities of G band to 2D band (I_G/I_{2D}) is an indicative of the number of layers in GNPs [63]. An increase in I_G/I_{2D} relates to stacking of carbon layers in GNPs.

The I_{2D}/I_G of GNPs gradually increased during the composite processing as shown in Table 1 which is mainly due to enhanced interactions between individual GNPs [80].

3.3. Microstructure of sintered samples

Fig. 6 shows OM micrographs of the sintered samples of pure Mg, Mg-0.5Zr, and MMNC and corresponding SEM images. It can be seen in OM images that pure Mg exhibited very clear grain boundaries with relatively large grain size (Fig. 6a), whereas the addition of Zr and GNPs significantly reduced the grain size of the Mg matrix (Fig. 6b and c). The grain sizes of the sintered samples were 16, 23, and 43 μm for the MMNC, Mg-0.5Zr, and pure Mg, respectively (see Table 2). It can be seen that the MMNC exhibited the smallest grain size among all the sintered samples, which is consistent with the results reported in a previous study [81]. It is worth noting that the SEM images of the sintered samples showed pores as indicated by the red arrows. However, the GNP-containing MMNC revealed a smaller size of pores compared to the pure Mg and Mg-0.5Zr samples (Fig. 6c; SEM). The average relative densities of the pure Mg, Mg-0.5Zr, and MMNC were measured as 92%, 94%, and 97%, respectively. The lower porosity of the GNP-containing MMNC may be attributable to the enhanced interfacial bonding between the GNPs and Mg matrix, which is beneficial in inhibiting grain growth at a high sintering temperature [82].

Fig. 7 shows SEM images and corresponding EDX elemental maps of the sintered samples of pure Mg, Mg-0.5Zr, and MMNC, revealing the distributions of Zr, GNPs, and O_2 in the Mg matrices. Fig. 7b shows an inhomogeneous distribution of some unalloyed Zr particles in the Mg matrices in the Mg-0.5Zr. It was reported that the inhomogeneous distribution of Zr particles adversely affects the

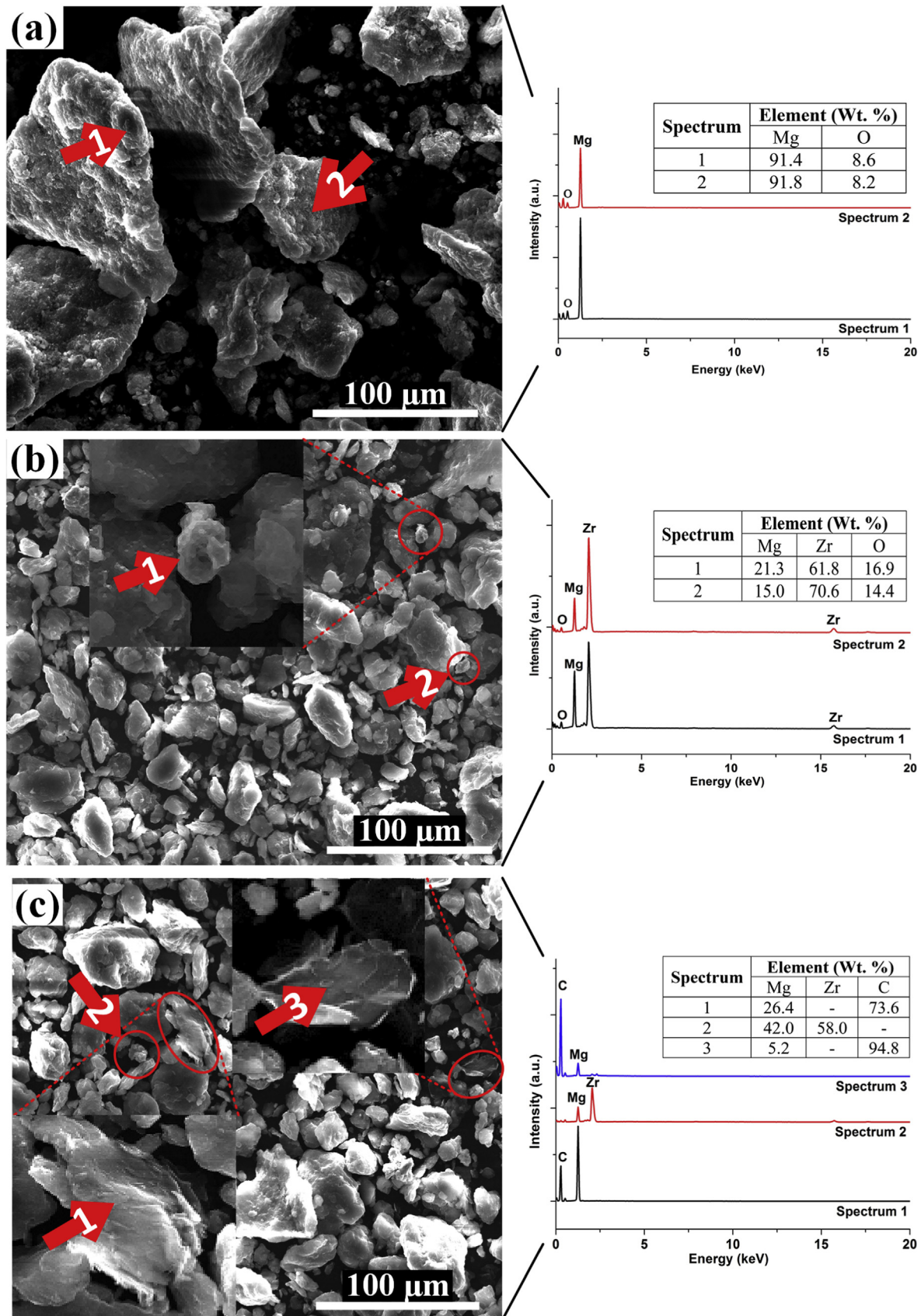


Fig. 3. SEM images of ball-milled pure Mg, Mg–Zr, and Mg–Zr–GNP powder mixtures and corresponding EDX analysis results: (a) pure Mg; (b) Mg–0.5Zr with inset showing enlarged image of dispersed Zr particle; and (c) Mg–0.5Zr–0.1GNPs with inset showing enlarged image of dispersed GNP in Mg powder matrix (red arrows indicate specific points from where EDX spectra were obtained). (For interpretation of the references to colour in this figure legend, the reader is referred to the Web version of this article.)

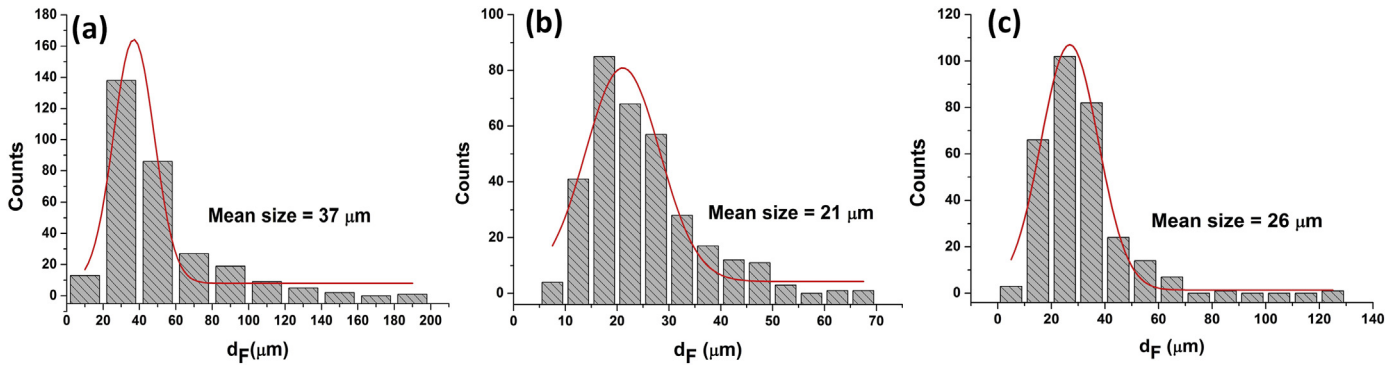


Fig. 4. Particle size distributions of ball-milled powders: (a) pure Mg; (b) Mg-0.5Zr; and (c) Mg-0.5Zr-0.1GNPs.

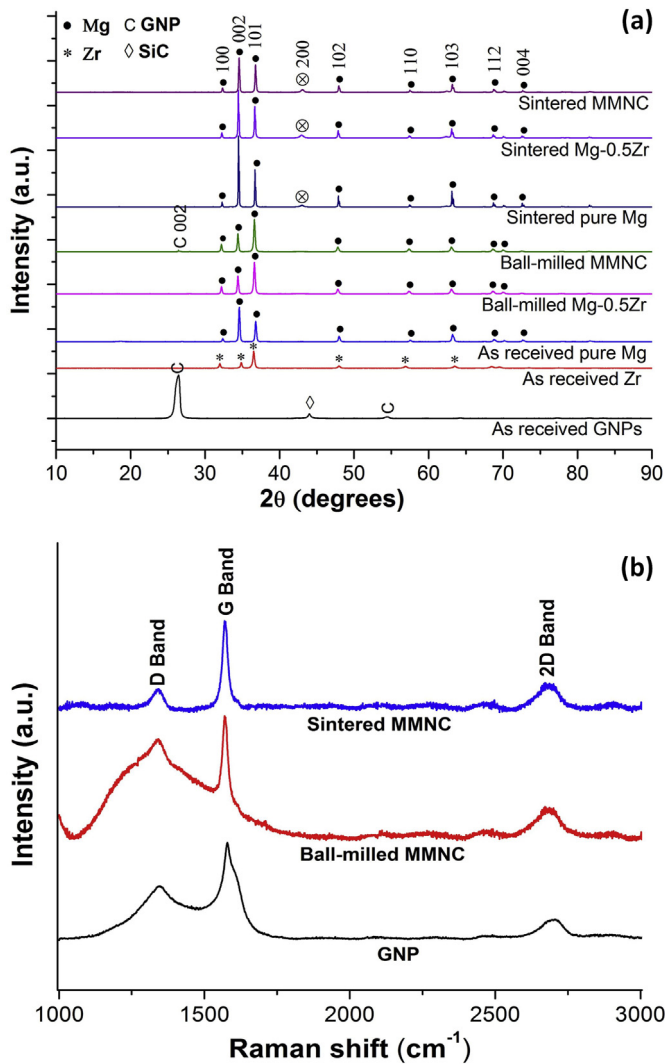


Fig. 5. (a) XRD patterns of as-received powders, ball-milled powder mixtures, and sintered samples; (b) Raman spectra of raw GNPs, ball-milled composite powder, and sintered MMNC.

mechanical and corrosion properties of Mg alloys [83]. Similarly, poor distribution of Zr was observed in the MMNC, whereas the distribution of carbon representing the GNPs was more uniform compared to Zr (Fig. 7c), indicating the effectiveness of the HEBM process in achieving uniform dispersion of GNPs in Mg matrices [69].

Table 1

Raman data of raw GNPs and their related products (average values are reported).

| Peak info | Raw GNP | Ball-milled Mg–Zr-GNPs powder | MMNC |
|-------------------------|---------|-------------------------------|------|
| I_D/I_G | 0.54 | 0.81 | 0.21 |
| I_{2D}/I_G | 0.21 | 0.25 | 0.30 |
| G (cm^{-1}) | 1578 | 1569 | 1571 |
| 2D (cm^{-1}) | 2705 | 2671 | 2668 |

3.4. Mechanical properties of sintered samples

Fig. 8a shows the nanoindentation load-displacement curves for the sintered samples of pure Mg, Mg-0.5Zr, and MMNC. The nano-hardness of Mg-0.5Zr and MMNC samples was measured as 50% and 100% higher than that of pure Mg (0.4 GPa), respectively. Whereas, the elastic modulus of MMNC was measured as 40% and 13% higher than those of pure Mg (25 GPa) and Mg-0.5Zr (31 GPa), respectively. This may be attributable to the load-transfer from the Mg matrix to the stiffer GNP reinforcements ($E_{\text{GNPs}} = 1 \text{ TPa}$) via the Mg–GNP interfaces [84]. The mechanical properties of the sintered samples of pure Mg, Mg-0.5Zr, and MMNC were also evaluated by compression tests as shown in Fig. 8b. It can be seen that the addition of Zr and GNPs enhanced the compressive yield strength (σ_{CYS}) and the ultimate compressive strength (σ_{UCS}) of the Mg matrices.

Table 2 lists the grain sizes, compressive properties, nano-indentation properties, and microhardnesses of the sintered samples of pure Mg, Mg-0.5Zr, and MMNC. The σ_{UCS} was 142, 181, and 219 MPa for the pure Mg, Mg-0.5Zr, and MMNC, respectively. The σ_{UCS} of the MMNC increased by 54% and 21% as compared to pure Mg and Mg-0.5Zr, respectively. The σ_{CYS} was 85, 145, and 162 MPa for the pure Mg, Mg-0.5Zr, and MMNC, respectively. The σ_{CYS} of the Mg-0.5Zr and MMNC was larger by 71% and 91%, respectively than the pure Mg. This may be attributable to the difference in atomic size between the alloying element and base metal, resulting in an interstitial solid solution effect [85]. The compressive strain (ϵ_c) of the pure Mg, Mg-0.5Zr, and MMNC was 9%, 5%, and 6%, respectively. It can be seen that the ϵ_c of the MMNC was lower than that of pure Mg. This may be attributable to dispersed GNPs in the Mg matrix which formed steric obstacles to dislocation in the MMNC during compressive load, resulting in an increase in resistance to deformation [86–88]. The addition of Zr and GNPs enhanced the nano-hardness and microhardness of the Mg matrices. The nano-hardness of pure Mg, Mg-0.5Zr, and MMNC was 25 GPa, 31 GPa, and 35 GPa, respectively. Similarly, the MMNC exhibited 26% and 23% higher Vicker hardness (HV), respectively, compared to pure Mg (46 HV) and Mg-0.5Zr (47 HV). Overall, the addition of GNPs to the Mg matrices improved their mechanical properties via synergistic strengthening mechanisms, which will be discussed below.

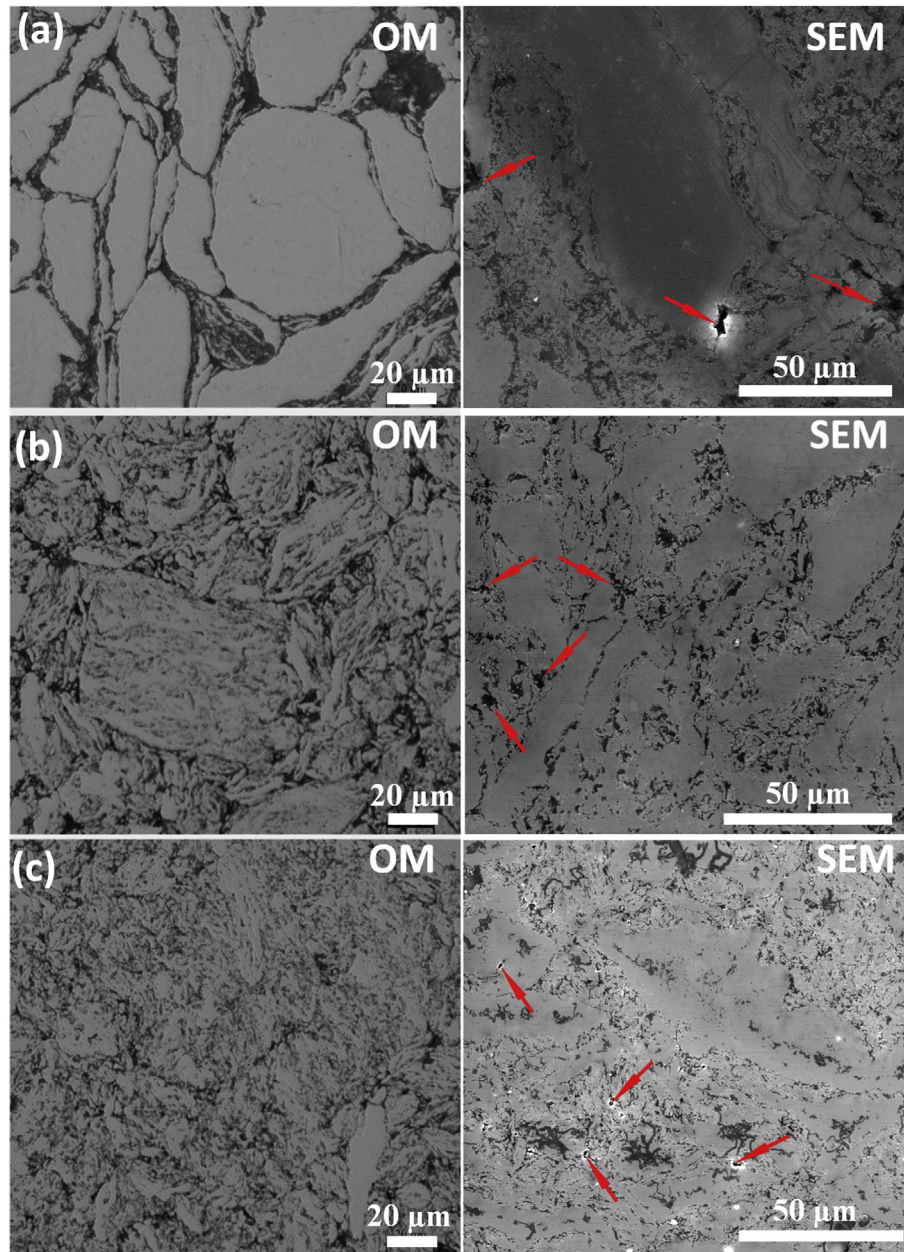


Fig. 6. OM micrographs and SEM images of sintered samples: (a) pure Mg; (b) Mg-0.5Zr; and (c) MMNC (red arrows indicating the formation of pores in these samples). (For interpretation of the references to colour in this figure legend, the reader is referred to the Web version of this article.)

Table 2
Mechanical properties of sintered samples evaluated by compression and nano-mechanical tests.

| Sample | Grain size (μm) | Compressive properties | | | Nano-mechanical properties | | Microhardness HV |
|----------|------------------------------|-----------------------------|-----------------------------|------------------|----------------------------|-------------------------|------------------|
| | | σ_{UCS} (MPa) | σ_{CYS} (MPa) | ϵ_c (%) | E_{nano} (GPa) | H_{nano} (GPa) | |
| Pure Mg | 43 ± 4 | 142 ± 4 | 85 ± 3 | 9 ± 2 | 25 ± 2 | 0.4 ± 0.1 | 46 ± 2 |
| Mg-0.5Zr | 23 ± 2 | 181 ± 4 | 145 ± 2 | 5 ± 2 | 31 ± 3 | 0.6 ± 0.1 | 47 ± 2 |
| MMNC | 16 ± 2 | 219 ± 3 | 162 ± 2 | 6 ± 2 | 35 ± 2 | 0.8 ± 0.1 | 58 ± 2 |

σ_{UCS} : ultimate compressive strength; σ_{CYS} : 0.2% compressive yield strength; ϵ_c : compressive strain; E_{nano} : elastic modulus; H_{nano} : hardness; HV: Vickers hardness.

3.5. Corrosion behavior of sintered samples

Fig. 9a shows polarization curves obtained from the electrochemical tests of the pure Mg, Mg-0.5Zr, and MMNC. During cathodic polarization, the MMNC showed better passivation up

to -0.3 V as compared to -1.0 V and -0.5 V in the Mg-0.5Zr and pure Mg samples, respectively. The polarization curve for the MMNC shows a decrease in current density (-2.8 mA/cm²) as compared to the Mg-0.5Zr (-2.1 mA/cm²) and pure Mg (-1.8 mA/cm²), indicating better corrosion resistance (Fig. 9a). A strong,

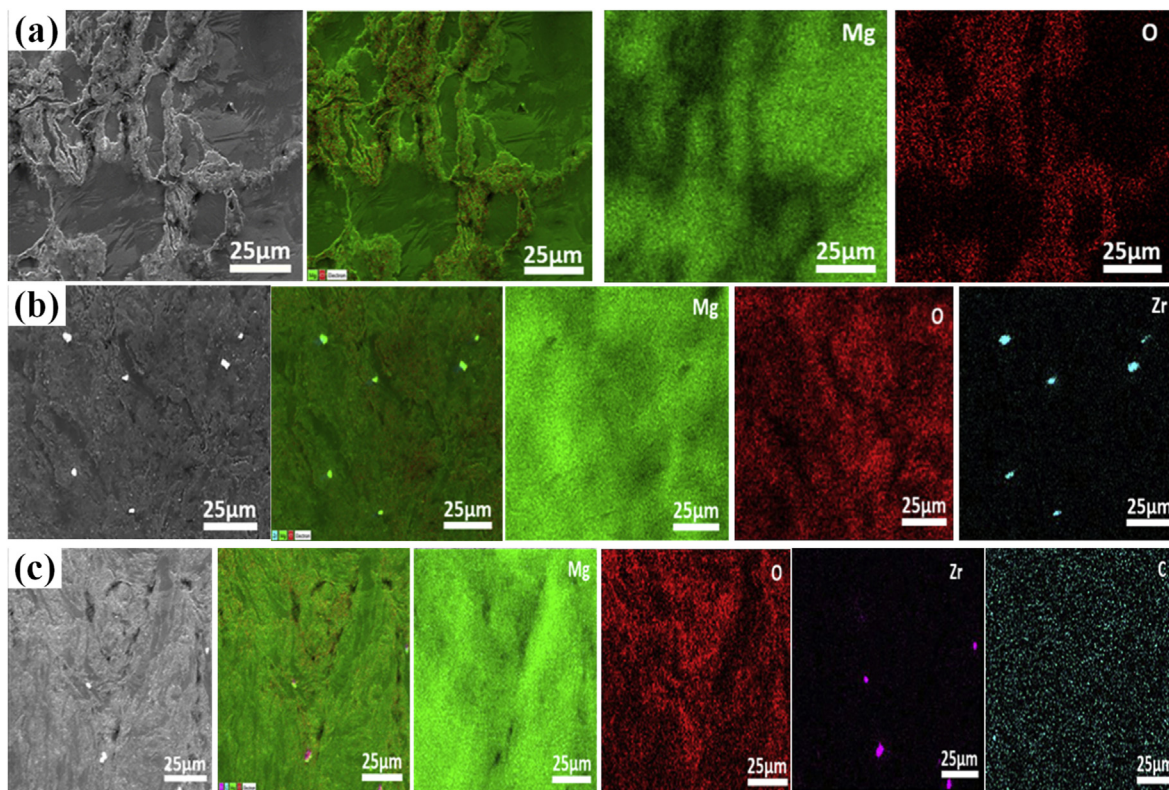


Fig. 7. SEM images and corresponding EDX maps showing distributions of reinforced Zr and GNPs and subsequent oxidation of Mg matrices: (a) pure Mg; (b) Mg-0.5Zr; and (c) MMNC.

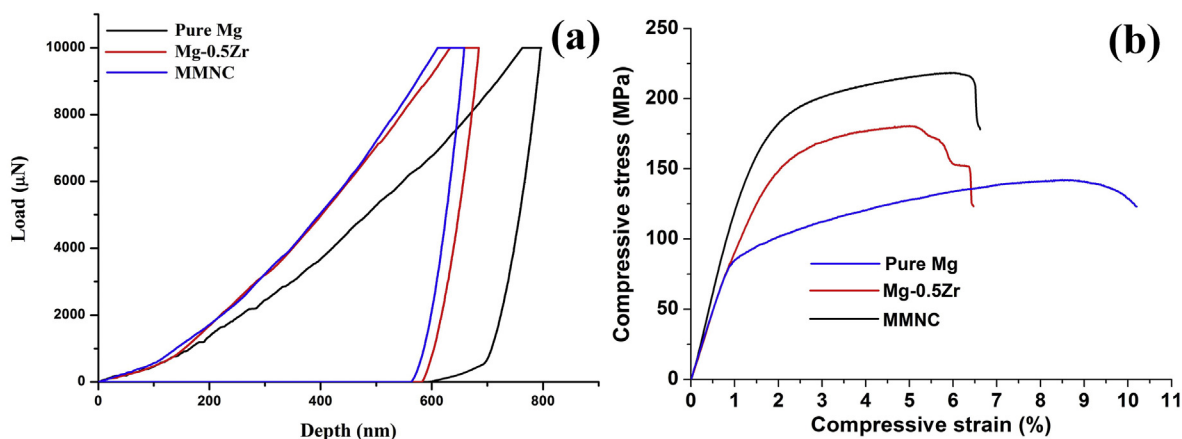


Fig. 8. Mechanical properties of sintered samples of pure Mg, Mg-0.5Zr, and MMNC: (a) nanoindentation load-displacement curves; and (b) compressive stress-strain curves.

uneven pitting effect was observed in the pure Mg and Mg-0.5Zr due to the breakdown of the passive film in the early stage, whereas the MMNC exhibited relatively uniform pitting corrosion. The current densities (I_{corr}) and resultant corrosion rates (CR) of the pure Mg, Mg-0.5Zr, and MMNC are summarized in Fig. 9b. Generally, a lower I_{corr} in potentiodynamic polarization testing indicates a higher corrosion resistance [89,90]. In this context, the MMNC exhibited a lower CR (11 mm y^{-1}) as compared to the Mg-0.5Zr (19 mm y^{-1}) and pure Mg (21 mm y^{-1}). It can be seen that the I_{corr} and CR of the MMNC were 48% lower than that of pure Mg, indicating good corrosion inhibition ability of the GNPs in the Mg matrices. The corresponding values for the corrosion potential (E_{corr}) and I_{corr} of the pure Mg, Mg-0.5Zr, and MMNC are

summarized in Table 3.

H_2 evolution vs immersion time curves for the sintered samples of pure Mg, Mg-0.5Zr, and MMNC in HBSS are shown in Fig. 9c. Compared to the pure Mg and Mg-0.5Zr samples, the MMNC showed the lowest H_2 evolution. The CR of the sintered samples of pure Mg, Mg-0.5Zr, and MMNC measured by both weight loss and H_2 evolution is shown in Fig. 9d. In the case of the CR for the pure Mg, Mg-0.5Zr, and MMNC, the weight-loss and H_2 evolution tests revealed 5.5, 4.5, and 3.0 mm y^{-1} and 19, 12, and 6 mm y^{-1} , respectively. It can be seen that the CR from both weight-loss and H_2 evolution measurements revealed a significant reduction in CR in the MMNC as compared to the pure Mg and Mg-0.5Zr. From the perspective of the corrosion inhibition ability of GNPs, recent

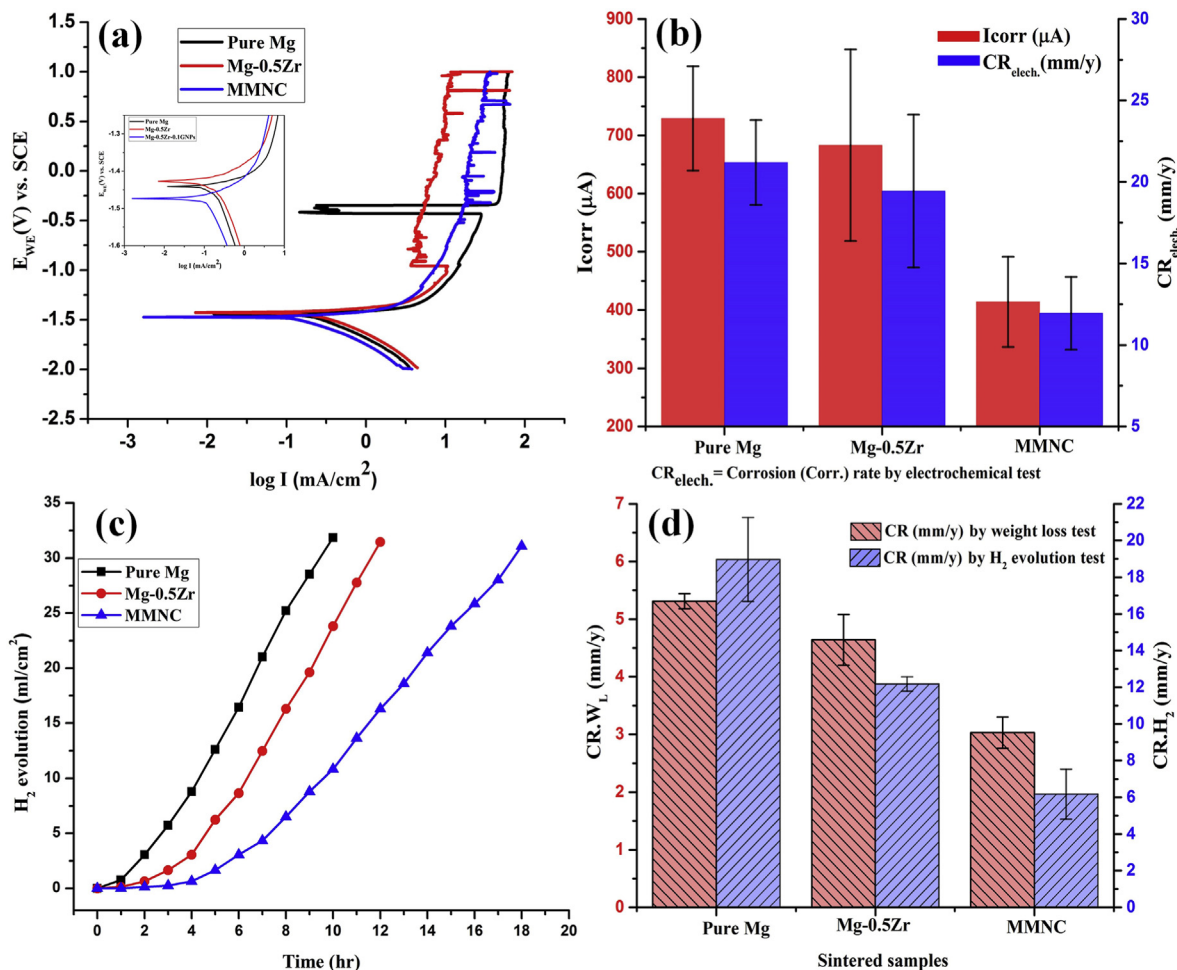


Fig. 9. Corrosion behavior of pure Mg, Mg-0.5Zr, and MMNC via electrochemical, H₂ evolution, and weight-loss tests in HBSS at 37 °C: (a) potentiodynamic polarization curves; (b) I_{corr} and CR_{elect} ; (c) H₂ evolution vs immersion time; (d) CR_{H_2} (measured from H₂ evolution) and CR_{WL} (measured from weight loss).

Table 3

Electrochemical corrosion potential (E_{corr}) and current density (I_{corr}) of pure Mg, Mg-0.5Zr, and MMNC.

| Sample | E_{corr} (mV) | I_{corr} (μA) |
|----------|------------------------|-------------------------------------|
| Pure Mg | -1624.5 ± 21.0 | 729.1 ± 29.6 |
| Mg-0.5Zr | -1602.4 ± 26.0 | 683.1 ± 24.6 |
| MMNC | -1595.9 ± 11.5 | 414.1 ± 27.2 |

studies suggested that a single atomic layer of GNPs consisting of sp^2 -C bonds was impermeable to gas molecules and provided an atomic-scale barrier in such a way that not even helium gas could pass through it [51,52,91,92]. Grain refinement of Mg matrices by the addition of uniformly dispersed GNPs is another factor that reduces the CR of MMNC [83].

Fig. 10a shows XRD patterns of the corroded samples after immersion in HBSS for 24 h at 37 °C. Compared to the pure Mg, the XRD pattern of the MMNC revealed a higher intensity of the Mg peak (101) at 36.62° in a same-lattice plane, indicating the corrosion inhibition ability of GNPs in Mg matrices. In addition to Mg peaks, XRD patterns of the corroded pure Mg, Mg-0.5Zr, and MMNC samples revealed additional peaks associated with $\text{Mg}(\text{OH})_2$ which were formed on the substrates as a corrosion product. It was reported that the overall corrosion mechanism of Mg and the

formation of corrosion products were governed by the reactions given by Ref. [93]:



The peak intensity of $\text{Mg}(\text{OH})_2$ for the three samples varied in the order pure Mg > Mg-0.5Zr > MMNC. The lower intensity of $\text{Mg}(\text{OH})_2$ in the MMNC may be attributable to the higher corrosion resistance of the GNP-reinforced Mg matrices, as fewer corrosion products of $\text{Mg}(\text{OH})_2$ deposited on the surface leads to a lower intensity of $\text{Mg}(\text{OH})_2$ peaks [94].

The concentration of Mg^{2+} ions in HBSS represented the release of Mg^{2+} ions from the immersed samples during their biodegradation. The Mg^{2+} ion concentration in HBSS was 8.0, 7.8, and 6.2 for the pure Mg, Mg-0.5Zr, and MMNC, respectively. The MMNC revealed the lowest Mg ion concentration as compared to the pure Mg and Mg-0.5Zr samples (Fig. 10b), indicating its highest corrosion resistance.

Fig. 11 shows the morphologies of the corroded surfaces of the three sintered samples of pure Mg, Mg-0.5Zr, and MMNC after immersion in HBSS for 24 h. Pitting corrosion was observed in the pure Mg sample which led to the formation of corrosion cracks, as shown in Fig. 11a. A thick film of corrosion products as indicated by the red arrow formed on the pure Mg sample, whereas the Mg-0.5Zr showed thin cracks as indicated by the white arrow, smaller

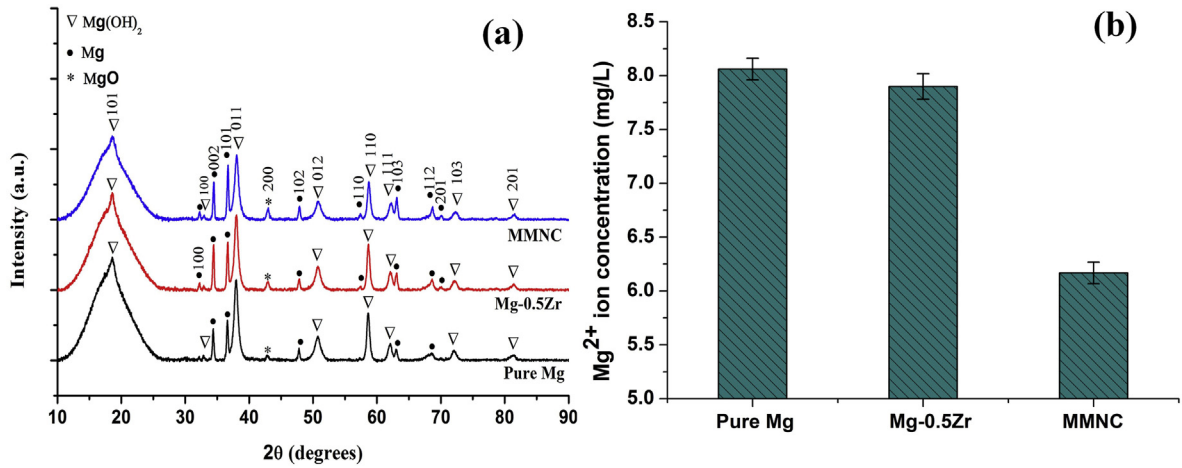


Fig. 10. XRD patterns of corroded samples and Mg ion release after 24 h immersion in HBSS: (a) XRD patterns obtained from corroded samples; and (b) corresponding Mg²⁺ ion concentrations in HBSS.

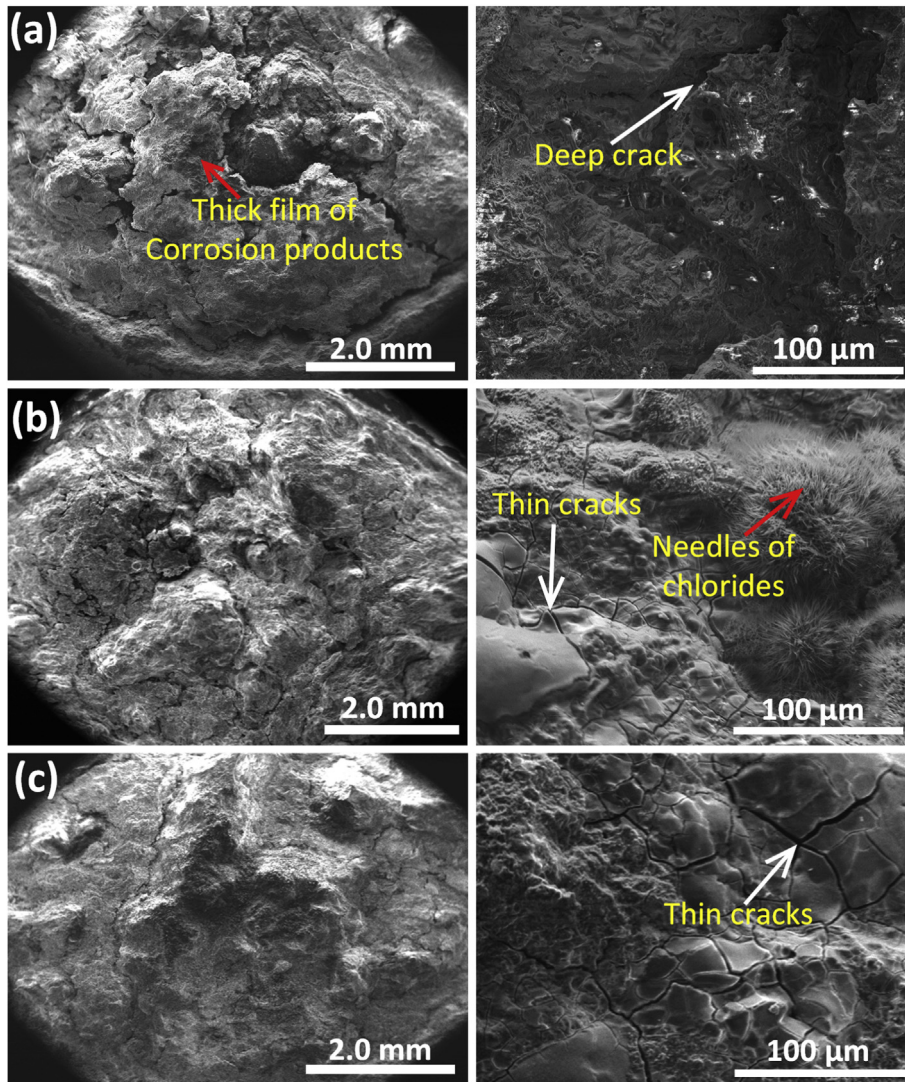


Fig. 11. Corrosion morphologies of sintered samples after immersion in HBSS for 24 h at 37 °C: (a) pure Mg; (b) Mg-0.5Zr; and (c) MMNC.

corrosion pits, and the presence of needle-shaped chlorides as indicated by the red arrow (Fig. 11b). It was reported that the presence of such needle-shaped chlorides in an Mg matrix breaks down the corrosion films on the surface, leading to the formation of deeper corrosion pits [94]. Compared to the pure Mg and Mg-0.5Zr samples, only a few corrosion pits formed on the MMNC (Fig. 11c).

3.6. Strengthening mechanisms of MMNCs

It has been reported that increases in the yield strength and ultimate strength of MMNCs by addition of reinforcing particles may be attributable to synergetic strengthening mechanisms including (i) grain-refinement (GR) strengthening [95]; (ii) difference in thermal expansion (DTE) strengthening; (iii) difference in elastic modulus (DEM) strengthening; (iv) geometric mismatch (GM) of Mg particles and GNPs; (v) load-transfer (LT) strengthening; and (vi) precipitation strengthening (PS) mechanisms [70,96]. The contribution of each strengthening mechanism to the yield strength of GNP-reinforced MMNCs can be calculated using the mathematical equations shown in Table 4.

DTE and DEM between the metal matrix and reinforcement may contribute to the yield strength of Mg matrices [46]. Fig. 12a shows the phenomenon of earlier expansion of Mg particles during high-temperature sintering due to their higher thermal expansion coefficient ($26 \times 10^{-6}/^{\circ}\text{K}$) [42] in all directions compared to GNPs (1.0×10^{-6}) (parallel to the surface) [70]. Fig. 12b shows the uniform dispersion of GNPs in the thermally expanded Mg matrix. This difference in thermal expansion between the Mg matrix and GNPs may also trigger the wrinkling of GNPs [107] (Fig. 12c). This can further resist dislocation motion in the Mg matrix during plastic deformation [108,109]. The addition of Zr and GNP particles to MMNCs inhibits the grain growth of the

Mg matrix by providing a pinning effect on its grain boundaries [24,110].

According to the Orowan theory [111], when a dislocation line passes through the non-coherent precipitates formed by reinforcing particles separated by interparticle distance (λ), the back stress produced by that precipitates on the dislocation line, leading to resistance to further dislocation motion during applied load. In this context, the precipitation of reinforcing particles in Mg matrices enhances the back stress, which can further resist dislocation motion during plastic deformation, leading to an increase in the yield strength of Mg matrices.

The LT from the Mg matrix to the reinforcing particles relies heavily on their interfacial bonding with the surrounding metal matrices [112]. The uniform dispersion of GNPs as reinforcing particles in the Mg matrices carries the potential for an effective load transfer from the Mg matrix to the GNPs during applied load (Fig. 12d), leading to an enhancement of load-carrying ability and resulting in an increase in the strength of the Mg matrices.

The geometrical mismatch between the Mg and Zr powders (irregular shapes) along with the two-dimensional GNPs leads to the generation of necessary dislocation motions during deformation, resulting in strain hardening of the MMNC. Fig. 13a shows the contribution of various strengthening mechanisms to the σ_{CYS} of the fabricated MMNC. DTE, GR, and LT were the most dominant strengthening mechanisms in the increased σ_{CYS} of the MMNC in this study. The σ_{CYS} of MMNC was also predicted using the Clyne method (Fig. 13b) [113] by considering the abovementioned strengthening mechanisms and was compared with the experimental results. The predicted yield strength was 164 MPa and the experiment revealed 162 MPa for the MMNC. It can be seen that the predicted and experimental results were in close agreement, showing the validity of these synergetic strengthening mechanisms in GNP-reinforced MMNCs.

Table 4
Various strengthening mechanisms and their mathematical equations for GNP-reinforced MMNCs as summarized from previous studies.

| Strengthening mechanism | Mathematical expressions | Variables and constants | References |
|---------------------------------|--|--|-----------------|
| Difference in thermal expansion | $\Delta\sigma_{\text{DTE}} = M\alpha_{\text{DTE}}G_{\text{Mg}}b\sqrt{Q_{\text{DTE}}}$ Where $Q_{\text{DTE}} = \frac{A\Delta T\Delta H\nu_f}{bd_p(1-\nu_f)}$ | M: Taylor orientation factor during thermal expansion ($\sqrt{3}$) α : Strengthening coefficient (1.25 for DTE and DG, 0.5 for DEM) A: Geometric constant (12) ΔT : Difference between processing and room temperature (K^{-1}) ΔH : DTE between matrix and reinforcing particle (K^{-1}) ν_f : Volume fraction of GNPs | [24,96 -102] |
| Difference in elastic modulus | $\Delta\sigma_{\text{DEM}} = \sqrt{3}\alpha_{\text{DEM}}G_{\text{Mg}}b\sqrt{Q_{\text{DEM}}}$ Where $Q_{\text{DEM}} = \frac{6\nu_f e}{\pi d_p^2}$ | ϵ : Deformation (m) λ : Inter-particle spacing of GNPs (m) γ_{Mg} : Shear strain in Mg matrix Q: Density of dislocation (m^{-2}) dp: Mean size of GNPs (m) | [97 -99,102] |
| Precipitation strengthening | $\Delta\sigma_{\text{Orowan}} = \frac{0.13G_{\text{Mg}}b}{\lambda} \ln\left(\frac{d_p}{2b}\right)$ Where $\lambda = d_p \left[\left(\frac{1}{2\nu_f}\right)^{\frac{1}{3}} - 1 \right]$ | E: Elastic modulus (GPa) G_{Mg} : Shear modulus of Mg matrix (1.66×10^4 MPa) b: Burgers vector of Mg (3.21×10^{-10} m) ν : Poisson's ratio of Mg (0.35) σ : Yield strength (MPa) τ : Shear stress during CRSS in basal slip (1.5 MPa) V_0 : Overall resistance (MPa) of lattice to dislocation movement for Mg (11) K_y : Strengthening coefficient or locking parameter due to GR (0.21 $\text{MPa}\sqrt{\text{m}}$ for pure Mg) d_g : Mean grain size (m) | [96,97,102] |
| Load transfer | $\Delta\sigma_{\text{LT}} = \frac{\nu_f\sigma_{\text{Mg}}}{2}$ | | [3,103] |
| Difference in geometry | $\Delta\sigma_{\text{DG}} = \alpha_{\text{DG}}G_{\text{Mg}}b\sqrt{\frac{8\nu_f\gamma_{\text{Mg}}}{bd_p}}$ Where $\gamma_{\text{Mg}} = \frac{\tau_{\text{CRSS}}}{G_{\text{Mg}}}$ | | [70,104] |
| Grain refinement | $\Delta\sigma_{\text{GR}} = \sigma_{\text{MMNC by GR}} - \sigma_{\text{Mg by GR}}$ Where $\sigma_{\text{GR}} = V_0 + \frac{K_y}{\sqrt{d_g}}$ | | [105,106] |

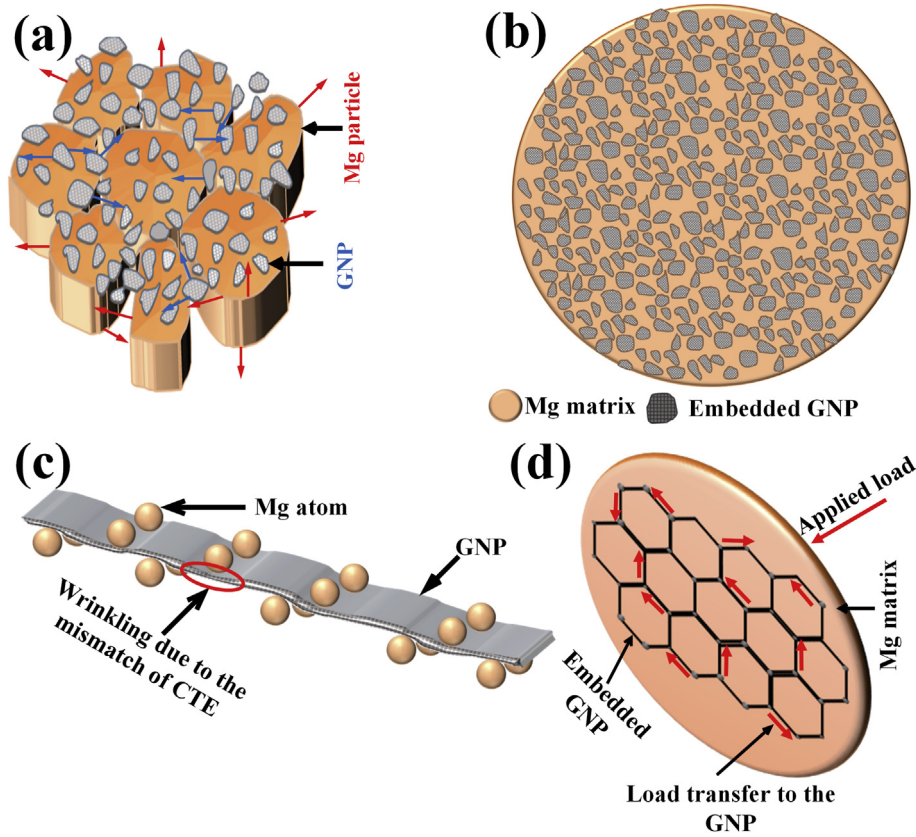


Fig. 12. DTE strengthening mechanism in GNP-reinforced Mg matrices: (a) difference in thermal expansion of Mg particles (red arrows) and GNPs (blue arrows); (b) dispersed GNPs in Mg matrix; (c) wrinkling of GNPs due to DTE between GNPs and Mg matrices; and (d) LT strengthening mechanism. (For interpretation of the references to colour in this figure legend, the reader is referred to the Web version of this article.)

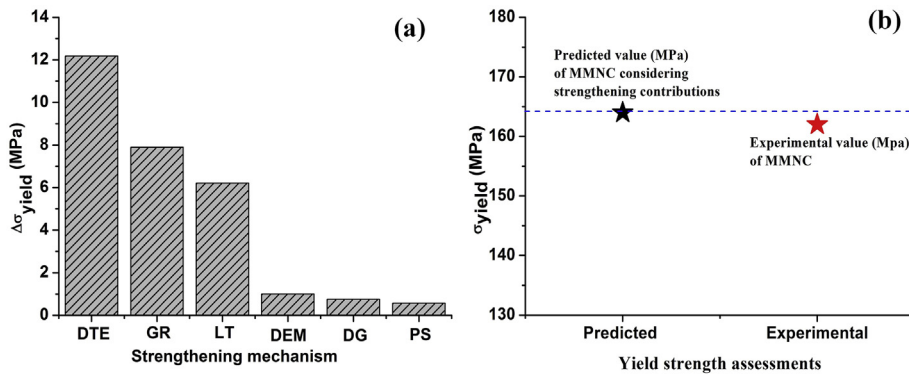


Fig. 13. Contributions and validity of various strengthening mechanisms to σ_{VCS} of GNP-reinforced MMNC: (a) contribution to yield strength ($\Delta\sigma_{yield}$) by individual strengthening mechanism, and (b) validation of predicted yield strength (MPa) (black star) considering possible strengthening mechanisms with experimental values (red star). (For interpretation of the references to colour in this figure legend, the reader is referred to the Web version of this article.)

4. Conclusions

In this study, an Mg-0.5Zr-0.1GNPs MMNC was synthesized via powder metallurgy. A homogenous dispersion of GNPs and Zr powders in the Mg powders was achieved by HEBM. As an alloying element, Zr provided a significant grain-refining effect to the MMNC, whereas the addition of GNPs to the Mg matrix enhanced its strength via various synergetic strengthening mechanisms including GR, DTE, DEM, GM, LT, and precipitation strengthening. Grain refinement of the Mg matrices by the addition of GNPs also

enhanced the corrosion resistance in HBSS. Based on the experimental results, the main conclusions of this study are as follows:

1. Addition of Zr and GNPs in Mg matrices significantly enhanced their mechanical properties via synergetic strengthening mechanisms.
2. The compressive yield strength, ultimate compressive strength, and hardness of Mg-Zr-GNP were higher than those of pure Mg and Mg-Zr samples, showing positive contribution of GNPs in enhancing the mechanical properties of Mg matrices.

- Uniform dispersion of GNPs in Mg matrices significantly reduced the H₂ evolution during their immersion in HBSS. Furthermore, electrochemical tests also revealed lower current densities and high corrosion resistance of MMNC compared to pure Mg and Mg–Zr samples.
- During immersion in HBSS, the concentration of Mg²⁺ ions was 8.0, 7.8, and 6.2 mg/L for the pure Mg, Mg-0.5Zr, and MMNC, respectively.
- The DTE, GR, and LT strengthening mechanisms were found to be the dominant mechanisms contributing to the enhanced σ_{CVS} and σ_{UCS} of the MMNCs.
- The predicted and experimental yield strength were in close agreement, confirming the validity of the considered synergetic strengthening mechanisms in GNP-reinforced MMNCs.
- Considering the positive contribution of GNPs in enhancing the mechanical and corrosion properties of pure Mg, this study encourages further studies to investigate their optimum concentrations in Mg matrices and the biocompatibility of MMNC.

Declaration of competing interest

The authors declare that they have no known competing financial interests or personal relationships that could have appeared to influence the work reported in this paper.

CRedit authorship contribution statement

Mohammad Shahin: Formal analysis, Data curation, Writing - original draft. **Khurram Munir:** Formal analysis, Data curation, Writing - review & editing. **Cuie Wen:** Conceptualization, Formal analysis, Data curation, Writing - review & editing, Conceptualization. **Yuncang Li:** Writing - review & editing, Conceptualization, Supervision.

Acknowledgment

The authors acknowledge the financial support for this research by the Australian Research Council (ARC) through the Future Fellowship (FT160100252) and the Discovery Project (DP170102557). The authors also thank the scientific and technical assistance of RMIT University's Microscopy and Microanalysis Facility (RMMF), a linked laboratory of the Australian Microscopy & Microanalysis Research Facility.

References

- Y. Xin, T. Hu, P. Chu, In vitro studies of biomedical magnesium alloys in a simulated physiological environment: a review, *Acta Biomater.* 7 (2011) 1452–1459, <https://doi.org/10.1016/j.actbio.2010.12.004>.
- F. Witte, N. Hort, C. Vogt, S. Cohen, K. Kainer, R. Willumeit, F. Feyerabend, Degradable biomaterials based on magnesium corrosion, *Curr. Opin. Solid State Mater. Sci.* 12 (2008) 63–72, <https://doi.org/10.1016/j.cossms.2009.04.001>.
- M. Shahin, K.S. Munir, C. Wen, Y. Li, Magnesium matrix nanocomposites for orthopedic applications: a review from mechanical, corrosion, and biological perspectives, *Acta Biomater.* 96 (2019) 1–19, <https://doi.org/10.1016/j.actbio.2019.06.007>.
- R. Zeng, W. Dietzel, F. Witte, N. Hort, C. Blawert, Progress and challenge for magnesium alloys as biomaterials, *Adv. Eng. Mater.* 10 (2008) 3–14, <https://doi.org/10.1002/adem.200800035>.
- F. Evans, The mechanical properties of bone, *Artif. Limbs* 13 (1969) 37–48.
- C. Wen, Y. Yamada, K. Shimojima, Y. Chino, H. Hosokawa, M. Mabuchi, Novel titanium foam for bone tissue engineering, *J. Mater. Res.* 17 (2002) 2633–2639, <https://doi.org/10.1557/JMR.2002.0382>.
- Y. Li, J. Xiong, P. Hodgson, C. Wen, Effects of structural property and surface modification of Ti6Ta4Sn scaffolds on the response of SaOS 2 cells for bone tissue engineering, *J. Alloys Compd.* 494 (2010) 323–329, <https://doi.org/10.1016/j.jallcom.2010.01.026>.
- A. Biesiekierski, D. Ping, Y. Li, J. Lin, K.S. Munir, Y. Yamabe-Mitarai, C. Wen, Extraordinary high strength Ti–Zr–Ta alloys through nanoscaled, dual-cubic spinodal reinforcement, *Acta Biomater.* 53 (2017) 549–558, <https://doi.org/10.1016/j.actbio.2017.01.085>.
- H. Liu, F. Cao, G. Song, D. Zheng, Z. Shi, M. Dargusch, A. Atrens, Review of the atmospheric corrosion of magnesium alloys, *J. Mater. Sci. Technol.* 35 (2019) 2003–2016, <https://doi.org/10.1016/j.jmst.2019.05.001>.
- Y. Xin, C. Liu, X. Zhang, G. Tang, X. Tian, P. Chu, Corrosion behavior of biomedical AZ91 magnesium alloy in simulated body fluids, *J. Mater. Res.* 22 (2007) 2004–2011, <https://doi.org/10.1557/jmr.2007.0233>.
- N. Li, Y. Zheng, Novel magnesium alloys developed for biomedical application: a review, *J. Mater. Sci. Technol.* 29 (2013) 489–502, <https://doi.org/10.1016/j.jmst.2013.02.005>.
- L. Mao, J. Chen, X. Zhang, M. Kwak, Y. Wu, R. Fan, L. Zhang, J. Pei, G. Yuan, C. Song, A promising biodegradable magnesium alloy suitable for clinical vascular stent application, *Sci. Rep.* 7 (2017) 1–12, <https://doi.org/10.1038/srep46343>.
- H. Martin, M. Horstemeyer, P. Wang, Structure–property quantification of corrosion pitting under immersion and salt-spray environments on an extruded AZ61 magnesium alloy, *Corrosion Sci.* 53 (2011) 1348–1361, <https://doi.org/10.1016/j.corsci.2010.12.025>.
- K. Törne, A. Örnberg, J. Weissenrieder, Influence of strain on the corrosion of magnesium alloys and zinc in physiological environments, *Acta Biomater.* 48 (2017) 541–550, <https://doi.org/10.1016/j.actbio.2016.10.030>.
- G. Song, A. Atrens, X. Wu, B. Zhang, Corrosion behaviour of AZ21, AZ501 and AZ91 in sodium chloride, *Corrosion Sci.* 40 (1998) 1769–1791, [https://doi.org/10.1016/S0010-938X\(98\)00078-X](https://doi.org/10.1016/S0010-938X(98)00078-X).
- S. Cai, T. Lei, N. Li, F. Feng, Effects of Zn on microstructure, mechanical properties and corrosion behavior of Mg–Zn alloys, *Mater. Sci. Eng. C* 32 (2012) 2570–2577, <https://doi.org/10.1016/j.msec.2012.07.042>.
- F. Czerwinski, *Corrosion of Materials in Liquid Magnesium Alloys and its Prevention, Magnesium Alloys: Properties in Solid and Liquid States*, 2014, pp. 131–170. Croatia.
- L. Christodoulou, H. Flower, Hydrogen embrittlement and trapping in Al6%–Zn3%–Mg, *Acta Metall.* 28 (1980) 481–487, [https://doi.org/10.1016/0001-6160\(80\)90138-8](https://doi.org/10.1016/0001-6160(80)90138-8).
- L. Mao, L. Shen, J. Niu, J. Zhang, W. Ding, Y. Wu, R. Fan, G. Yuan, Nanophase biodegradation enhances the durability and biocompatibility of magnesium alloys for the next-generation vascular stents, *Nanoscale* 5 (2013) 9517–9522, <https://doi.org/10.1039/C3NR02912C>.
- X. Zhang, G. Yuan, L. Mao, J. Niu, W. Ding, Biocorrosion properties of as-extruded Mg–Nd–Zn–Zr alloy compared with commercial AZ31 and WE43 alloys, *Mater. Lett.* 66 (2012) 209–211, <https://doi.org/10.1016/j.matlet.2011.08.079>.
- Z. Huan, M.A. Leeflang, J. Zhou, J. Duszczuk, ZK30–bioactive glass composites for orthopedic applications: a comparative study on fabrication method and characteristics, *Mater. Sci. Eng. B* 176 (2011) 1644–1652, <https://doi.org/10.1016/j.mseb.2011.07.022>.
- F. Witte, F. Feyerabend, P. Maier, J. Fischer, M. Störmer, C. Blawert, W. Dietzel, N. Hort, Biodegradable magnesium–hydroxyapatite metal matrix composites, *Biomaterials* 28 (2007) 2163–2174.
- L. Wu, X. Ding, Z. Zheng, Y. Ma, A. Atrens, X. Chen, Z. Xie, D. Sun, F. Pan, Fabrication and characterization of an actively protective Mg–Al LDHs/Al₂O₃ composite coating on magnesium alloy AZ31, *Appl. Surf. Sci.* 487 (2019) 558–568, <https://doi.org/10.1016/j.apsusc.2019.04.020>.
- Q. Nguyen, M. Gupta, Enhancing compressive response of AZ31B magnesium alloy using alumina nanoparticles, *Compos. Sci. Technol.* 68 (2008) 2185–2192, <https://doi.org/10.1016/j.compscitech.2008.04.020>.
- R. Radha, D. Sreekanth, Insight of magnesium alloys and composites for orthopedic implant applications—a review, *J. Magnes. Alloys* 5 (2017) 286–312, <https://doi.org/10.1016/j.jma.2017.08.003>.
- D. Liu, Y. Huang, P. Prangnell, Microstructure and performance of a biodegradable Mg–1Ca–2Zn–1TCP composite fabricated by combined solidification and deformation processing, *Mater. Lett.* 82 (2012) 7–9, <https://doi.org/10.1016/j.matlet.2012.05.035>.
- X. Ma, L. Dong, X. Wang, Microstructure, mechanical property and corrosion behavior of co-continuous β -TCP/MgCa composite manufactured by suction casting, *Mater. Des.* 56 (2014) 305–312, <https://doi.org/10.1016/j.matdes.2013.11.041>.
- K. Ralston, N. Birbilis, C. Davies, Revealing the relationship between grain size and corrosion rate of metals, *Scripta Mater.* 63 (2010) 1201–1204, <https://doi.org/10.1016/j.scriptamat.2010.08.035>.
- Y. Li, C. Wen, D. Mushahary, R. Sravanthi, N. Harishankar, G. Pande, P. Hodgson, Mg–Zr–Sr alloys as biodegradable implant materials, *Acta Biomater.* 8 (2012) 3177–3188, <https://doi.org/10.1016/j.actbio.2012.04.028>.
- Y. Ding, Y. Li, C. Wen, Effects of Mg17Sr2 phase on the bio-corrosion behavior of Mg–Zr–Sr alloys, *Adv. Eng. Mater.* 18 (2016) 259–268, <https://doi.org/10.1002/adem.201500222>.
- B. Cappel, S. Neuss, J. Salber, R. Telle, R. Knüchel, H. Fischer, Cytocompatibility of high strength non-oxide ceramics, *J. Biomed. Mater. Res. Part A* 93 (2010) 67–76, <https://doi.org/10.1002/jbm.a.32527>.
- C. Silva, B. König Jr., M. Carbonari, M. Yoshimoto, S. Allegrini Jr., J.C. Bressiani, Tissue response around silicon nitride implants in rabbits, *J. Biomed. Mater. Res. Part A* 84 (2008) 337–343, <https://doi.org/10.1002/jbm.a.31363>.
- M. Razavi, M. Fathi, M. Meratian, Fabrication and characterization of magnesium–fluorapatite nanocomposite for biomedical applications, *Mater.*

- Char. 61 (2010) 1363–1370, <https://doi.org/10.1016/j.matchar.2010.09.008>.
- [34] M. Razavi, M. Fathi, M. Meratian, Bio-corrosion behavior of magnesium-fluorapatite nanocomposite for biomedical applications, *Mater. Lett.* 64 (2010) 2487–2490, <https://doi.org/10.1016/j.matlet.2010.07.079>.
- [35] W. Paul, C. Sharma, Blood compatibility and biomedical applications of graphene, *Trends Biomater. Artif. Organs* 25 (2011) 91–94, <http://medind.nic.in/taat/t113/taat1113p91>.
- [36] S. Chinkanjanarot, J. Tomasi, J. King, G. Odegard, Thermal conductivity of graphene nanoplatelet/cycloaliphatic epoxy composites: Multiscale modeling, *Carbon* 140 (2018) 653–663, <https://doi.org/10.1016/j.carbon.2018.09.024>.
- [37] A. Saboori, S. Moheimani, M. Pavese, C. Badini, P. Fino, New nanocomposite materials with improved mechanical strength and tailored coefficient of thermal expansion for electro-packaging applications, *Metals* 7 (2017) 1–14, <https://doi.org/10.3390/met7120536>.
- [38] K. Munir, M. Qian, Y. Li, D.T. Oldfield, P. Kingshott, D. Zhu, C. Wen, Quantitative analyses of MWCNT-Ti powder mixtures using Raman spectroscopy: the influence of milling parameters on nanostructural evolution, *Adv. Eng. Mater.* 17 (2015) 1660–1669, <https://doi-org.ezproxy.lib.rmit.edu.au/10.1002/adem.201500142>.
- [39] L. Chen, H. Konishi, A. Fehrenbacher, C. Ma, J. Xu, H. Choi, H. Xu, F.E. Pfefferkorn, X.C. Li, Novel nanoprocessing route for bulk graphene nanoplatelets reinforced metal matrix nanocomposites, *Scripta Mater.* 67 (2012) 29–32, <https://doi.org/10.1016/j.scriptamat.2012.03.013>.
- [40] M. Rashad, F. Pan, A. Tang, Y. Lu, M. Asif, S. Hussain, J. She, J. Gou, J. Mao, Effect of graphene nanoplatelets (GNPs) addition on strength and ductility of magnesium-titanium alloys, *J. Magnes. Alloys* 1 (2013) 242–248, <https://doi.org/10.1016/j.jma.2013.09.004>.
- [41] M. Rashad, F. Pan, A. Tang, M. Asif, J. She, J. Gou, J. Mao, H. Hu, Development of magnesium-graphene nanoplatelets composite, *J. Compos. Mater.* 49 (2015) 285–293, <https://doi.org/10.1177/0021998313518360>.
- [42] M. Rashad, F. Pan, M. Asif, A. Tang, Powder metallurgy of Mg–1% Al–1% Sn alloy reinforced with low content of graphene nanoplatelets (GNPs), *J. Ind. Eng. Chem.* 20 (2014) 4250–4255, <https://doi.org/10.1016/j.jiec.2014.01.028>.
- [43] M. Rashad, F. Pan, A. Tang, M. Asif, M. Aamir, Synergetic effect of graphene nanoplatelets (GNPs) and multi-walled carbon nanotube (MW-CNTs) on mechanical properties of pure magnesium, *J. Alloys Compd.* 603 (2014) 111–118, <https://doi.org/10.1016/j.jallcom.2014.03.038>.
- [44] M. Rashad, F. Pan, H. Hu, M. Asif, S. Hussain, J. She, Enhanced tensile properties of magnesium composites reinforced with graphene nanoplatelets, *Mater. Sci. Eng., A* 630 (2015) 36–44, <https://doi.org/10.1016/j.msea.2015.02.002>.
- [45] M. Rashad, F. Pan, D. Lin, M. Asif, High temperature mechanical behavior of AZ61 magnesium alloy reinforced with graphene nanoplatelets, *Mater. Des.* 89 (2016) 1242–1250, <https://doi.org/10.1016/j.matdes.2015.10.101>.
- [46] M. Rashad, F. Pan, M. Asif, X. Chen, Corrosion behavior of magnesium-graphene composites in sodium chloride solutions, *J. Magnes. Alloys* 5 (2017) 271–276, <https://doi.org/10.1016/j.jma.2017.06.003>.
- [47] Z. Hu, G. Tong, D. Lin, C. Chen, H. Guo, J. Xu, L. Zhou, Graphene-reinforced metal matrix nanocomposites—a review, *Mater. Sci. Technol.* 32 (2016) 930–953, <https://doi.org/10.1080/02670836.2015.1104018>.
- [48] N. Saikrishna, G. Reddy, B. Munirathinam, B. Sunil, Influence of bimodal grain size distribution on the corrosion behavior of friction stir processed biodegradable AZ31 magnesium alloy, *J. Magnes. Alloys* 4 (2016) 68–76, <https://doi.org/10.1016/j.jma.2015.12.004>.
- [49] S. Böhm, Graphene against corrosion, *Nat. Nanotechnol.* 9 (2014) 741–742, <https://doi.org/10.1038/nnano.2014.220>.
- [50] N. Kirkland, T. Schiller, N. Medhekar, N. Birbilis, Exploring graphene as a corrosion protection barrier, *Corrosion Sci.* 56 (2012) 1–4, <https://doi.org/10.1016/j.corsci.2011.12.003>.
- [51] L. Tsetseris, S. Pantelides, Graphene: an impermeable or selectively permeable membrane for atomic species? *Carbon* 67 (2014) 58–63, <https://doi.org/10.1016/j.carbon.2013.09.055>.
- [52] K. Munir, C. Wen, Y. Li, Carbon nanotubes and graphene as nanoreinforcements in metallic biomaterials: a review, *Adv. Biosyst.* 3 (2019) 1–24, <https://doi.org/10.1002/adbi.201800212>.
- [53] R. Raman, P. Banerjee, D. Lobo, H. Gullapalli, M. Sumandasa, A. Kumar, L. Choudhary, R. Tkacz, P.M. Ajayan, M. Majumder, Protecting copper from electrochemical degradation by graphene coating, *Carbon* 50 (2012) 4040–4045, <https://doi.org/10.1016/j.carbon.2012.04.048>.
- [54] G. Kotchey, B. Allen, H. Vedala, N. Yamamala, A. Kapralov, Y. Tyurina, J. Klein-Seetharaman, V.E. Kagan, A. Star, The enzymatic oxidation of graphene oxide, *ACS Nano* 5 (2011) 2098–2108, <https://doi.org/10.1021/nn103265h>.
- [55] L. Newman, N. Lozano, M. Zhang, S. Iijima, M. Yudasaka, C. Bussy, K. Kostarelos, Hypochlorite degrades 2D graphene oxide sheets faster than 1D oxidised carbon nanotubes and nanohorns, *NPJ 2D Mater. Appl.* 1 (2017) 1–9, <https://doi.org/10.1038/s41699-017-0041-3>.
- [56] M. Neagu, Z. Piperigkou, K. Karamanou, A.B. Engin, A.O. Docea, C. Constantin, C. Negrei, D. Nikitovic, A. Tsatsakis, Protein bio-corona: critical issue in immune nanotoxicology, *Arch. Toxicol.* 91 (2017) 1031–1048, <https://doi.org/10.1007/s00204-016-1797-5>.
- [57] B. Girase, J. Shah, R. Misra, Cellular mechanics of modulated osteoblasts functions in graphene oxide reinforced elastomers, *Adv. Eng. Mater.* 14 (2012) 101–111, <https://doi.org/10.1002/adem.201180028>.
- [58] M. Hronik-Tupaj, W. Rice, M. Cronin-Golomb, D.L. Kaplan, I. Georgakoudi, Osteoblastic differentiation and stress response of human mesenchymal stem cells exposed to alternating current electric fields, *Biomed. Eng. Online* 10 (2011) 1–22, <https://doi.org/10.1186/1475-925X-10-9>.
- [59] R. Aaron, B. Boyan, D. Ciombor, Z. Schwartz, B. Simon, Stimulation of growth factor synthesis by electric and electromagnetic fields, *Clin. Orthop. Relat. Res.* 419 (2004) 30–37, <https://doi.org/10.1097/00003086-200402000-00006>.
- [60] W. La, M. Jin, S. Park, H. Yoon, G. Jeong, S. Bhang, H. Park, K. Char, B. Kim, Delivery of bone morphogenetic protein-2 and substance P using graphene oxide for bone regeneration, *Int. J. Nanomed.* 9 (2014) 107–116, <https://doi.org/10.2147/IJN.S50742>.
- [61] S. Ku, C. Park, Myoblast differentiation on graphene oxide, *Biomaterials* 34 (2013) 2017–2023, <https://doi.org/10.1016/j.biomaterials.2012.11.052>.
- [62] S. Pandit, Z. Cao, V.R. Mokkaapati, E. Celauro, A. Yurgens, M. Lovmar, F. Westerlund, J. Sun, I. Mijakovic, Vertically aligned graphene coating is bactericidal and prevents the formation of bacterial biofilms, *Adv. Mater. Interfaces* 5 (2018) 1–9, <https://doi.org/10.1002/admi.201701331>.
- [63] K. Munir, C. Wen, Y. Li, Graphene nanoplatelets-reinforced magnesium metal matrix nanocomposites with superior mechanical and corrosion performance for biomedical applications, *J. Magnes. Alloys* (2020), <https://doi.org/10.1016/j.jma.2019.12.002>.
- [64] A. Saberi, H. Bakhsheshi-Rad, E. Karamian, M. Kasiri-Asgarani, H. Ghomi, Magnesium-graphene nano-platelet composites: corrosion behavior, mechanical and biological properties, *J. Alloys Compd.* 821 (2020) 153379, <https://doi.org/10.1016/j.jallcom.2019.153379>.
- [65] D. StJohn, M. Qian, M. Easton, P. Cao, Z. Hildebrand, Grain refinement of magnesium alloys, *Metall. Mater. Trans. A* 36 (2005) 1669–1679, <https://doi.org/10.1007/s11661-005-0030-6>.
- [66] K. Gusieva, C. Davies, J. Scully, N. Birbilis, Corrosion of magnesium alloys: the role of alloying, *Int. Mater. Rev.* 60 (2015) 169–194, <https://doi.org/10.1179/1743280414Y.0000000046>.
- [67] J. Davidson, Zirconium Oxide and Zirconium Nitride Coated Biocompatible Leads, US Patent 5496359A, 1996.
- [68] Y. Zhao, M. Jimesh, W. Li, G. Wu, C. Wang, Y. Zheng, K. Yeung, P. Chu, Enhanced antimicrobial properties, cytocompatibility, and corrosion resistance of plasma-modified biodegradable magnesium alloys, *Acta Biomater.* 10 (2014) 544–556, <https://doi.org/10.1016/j.actbio.2013.10.012>.
- [69] K. Munir, Y. Li, J. Lin, C. Wen, Interdependencies between graphitization of carbon nanotubes and strengthening mechanisms in titanium matrix composites, *Materials* 3 (2018) 122–138, <https://doi.org/10.1016/j.mtla.2018.08.015>.
- [70] M. Rashad, F. Pan, A. Tang, M. Asif, S. Hussain, J. Gou, J. Mao, Improved strength and ductility of magnesium with addition of aluminum and graphene nanoplatelets (Al+ GNPs) using semi powder metallurgy method, *J. Ind. Eng. Chem.* 23 (2015) 243–250, <https://doi.org/10.1016/j.jiec.2014.08.024>.
- [71] W. Oliver, G. Pharr, Measurement of hardness and elastic modulus by instrumented indentation: Advances in understanding and refinements to methodology, *J. Mater. Res.* 19 (2004) 3–20, <https://doi.org/10.1557/jmr.2004.19.1.3>.
- [72] K. Herrmann, Hardness measurement of metals-static methods, in: K. Herrman (Ed.), *Hardness Testing: Principles and Applications*, ASM Int., USA, 2011, pp. 43–51.
- [73] A. Jennifer, A. Lorenzi, V. Foray, T. Hance, Impact of differences in nutritional quality of wingless and winged aphids on parasitoid fitness, *J. Exp. Biol.* 221 (2018) 1–11, <http://jeb.biologists.org/lookup/doi/10.1242/jeb.185645>.
- [74] A. Atrens, M. Liu, N. Zainal Abidin, Corrosion mechanism applicable to biodegradable magnesium implants, *Mater. Sci. Eng. B* 176 (2011) 1609–1636, <https://doi.org/10.1016/j.mseb.2010.12.017>.
- [75] S. Khalifeh, T.D. Burlleigh, Influence of Heat Treatment on the Corrosion Behavior of Purified Magnesium and AZ31 Alloy, Condensed Matter, Cornell University, 27 June 2017, pp. 1–23, <https://arxiv.org/abs/1706.08663>.
- [76] S. Zhang, X. Zhang, C. Zhao, J. Li, Y. Song, C. Xie, H. Tao, Y. Zhang, Y. He, Y. Jiang, Y. Bian, Research on an Mg-Zn alloy as a degradable biomaterial, *Acta Biomater.* 6 (2010) 626–640, <https://doi.org/10.1016/j.actbio.2009.06.028>.
- [77] H. Merkus, Particle size, size distributions and shape, in: H. Merkus (Ed.), *Particle Size Measurements: Fundamentals, Practice, Quality*, Springer Science & Business Media, Netherlands, 2009, pp. 14–41.
- [78] A. McNaught, A. Wilkinson, Compendium of Chemical Terminology, second ed., Blackwell Scientific Publications, Oxford, 1997 the "Gold Book".
- [79] J. Hubbell, S. Seltzer, Tables of X-Ray Mass Attenuation Coefficients and Mass Energy-Absorption Coefficients 1 keV to 20 MeV for Elements Z = 1 to 92 and 48 Additional Substances of Dosimetric Interest, U.S. Department of Energy, Office of Standard and Technical Information, 1995.
- [80] A. Gupta, G. Chen, P. Joshi, S. Tadigadapa, P. Eklund, Raman scattering from high-frequency phonons in supported n-graphene layer films, *Nano Lett.* 6 (2006) 2667–2673, <https://doi.org/10.1021/nl061420a>.
- [81] M. Rashad, F. Pan, M. Asif, A. Ullah, Improved mechanical properties of magnesium-graphene composites with copper-graphene hybrids, *Mater. Sci. Technol.* 31 (2015) 1452–1461, <https://doi.org/10.1179/1743284714Y.0000000726>.
- [82] W. Yang, W. Huang, Z. Wang, F. Shang, W. Huang, B. Zhang, Thermal and mechanical properties of graphene-titanium composites synthesized by microwave sintering, *Acta Metall. Si. (English Letters)* 29 (2016) 707–713, <https://doi.org/10.1007/s40195-016-0445-7>.

- [83] K. Munir, Y. Li, D. Liang, M. Qian, W. Xu, C. Wen, Effect of dispersion method on the deterioration, interfacial interactions and re-agglomeration of carbon nanotubes in titanium metal matrix composites, *Mater. Des.* 88 (2015) 138–148, <https://doi.org/10.1016/j.matdes.2015.08.112>.
- [84] Y. Yang, W. Rigdon, X. Huang, X. Li, Enhancing graphene reinforcing potential in composites by hydrogen passivation induced dispersion, *Sci. Rep.* 3 (2013) 1–7, <https://doi.org/10.1038/srep02086>.
- [85] A. Mouritz, Strengthening of metal alloys, in: A.P. Mouritz (Ed.), *Introduction to Aerospace Materials*, Woodhead publishing Ltd., UK, 2012, pp. 57–89.
- [86] H. Hugosson, U. Jansson, B. Johansson, O. Eriksson, Restricting dislocation movement in transition metal carbides by phase stability tuning, *Sci* 293 (2001) 2434–2437, <https://doi.org/10.1126/science.1060512>.
- [87] M. Rashad, F. Pan, A. Tang, M. Asif, M. Aamir, Synergetic effect of graphene nanoplatelets (GNPs) and multi-walled carbon nanotube (MW-CNTs) on mechanical properties of pure magnesium, *J. Alloys Compd.* 603 (2014) 111–118, <https://doi.org/10.1016/j.jallcom.2014.03.038>.
- [88] M. Russell-Stevens, R. Todd, M. Papakyriacou, Microstructural analysis of a carbon fibre reinforced AZ91D magnesium alloy composite, *Surf. Interface Anal.* 37 (2005) 336–342, <https://doi.org/10.1002/sia.2026>.
- [89] A. Sanchez, B. Luthringer, F. Feyerabend, R. Willumeit, Mg and Mg alloys: how comparable are in vitro and in vivo corrosion rates? a review, *Acta Biomater.* 13 (2015) 16–31, <https://doi.org/10.1016/j.actbio.2014.11.048>.
- [90] J. Niu, G. Yuan, Y. Liao, L. Mao, J. Zhang, Y. Wang, F. Huang, Y. Jiang, Y. He, W. Ding, Enhanced biocorrosion resistance and biocompatibility of degradable Mg–Nd–Zn–Zr alloy by brushite coating, *Mater. Sci. Eng. C* 33 (2013) 4833–4841, <https://doi.org/10.1016/j.msec.2013.08.008>.
- [91] J. Bunch, S. Verbridge, J. Alden, A. Van Der Zande, J. Parpia, H. Craighead, P. McEuen, Impermeable atomic membranes from graphene sheets, *Nano Lett.* 8 (2008) 2458–2462, <https://doi.org/10.1021/nl801457b>.
- [92] J. Schrier, Helium separation using porous graphene membranes, *J. Phys. Chem. Lett.* 1 (2010) 2284–2287, <https://doi.org/10.1021/jz100748x>.
- [93] A. Atrens, G. Song, M. Liu, Z. Shi, F. Cao, M. Dargusch, Review of recent developments in the field of magnesium corrosion, *Adv. Eng. Mater.* 17 (2015) 400–453, <https://doi.org/10.1002/adem.201400434>.
- [94] R. Zeng, X. Li, S. Li, F. Zhang, E. Han, In vitro degradation of pure Mg in response to glucose, *Sci. Rep.* 5 (2015) 1–14, <https://doi.org/10.1038/srep13026>.
- [95] D. Witkin, Z. Lee, R. Rodriguez, S. Nutt, E. Lavernia, Al–Mg alloy engineered with bimodal grain size for high strength and increased ductility, *Scripta Mater.* 49 (2003) 297–302, [https://doi.org/10.1016/S1359-6462\(03\)00283-5](https://doi.org/10.1016/S1359-6462(03)00283-5).
- [96] A. Sanaty-Zadeh, Comparison between current models for the strength of particulate-reinforced metal matrix nanocomposites with emphasis on consideration of Hall–Petch effect, *Mater. Sci. Eng., A* 531 (2012) 112–118, <https://doi.org/10.1016/j.msea.2011.10.043>.
- [97] R. Casati, M. Vedani, Metal matrix composites reinforced by nano-particles—a review, *Metals* 4 (2014) 65–83, <https://doi.org/10.3390/met4010065>.
- [98] S. Hassan, M. Tan, M. Gupta, High-temperature tensile properties of Mg/Al2O3 nanocomposite, *Mater. Sci. Eng., A* 486 (2008) 56–62, <https://doi.org/10.1016/j.msea.2007.08.045>.
- [99] K. Tun, M. Gupta, Improving mechanical properties of magnesium using nano-yttria reinforcement and microwave assisted powder metallurgy method, *Compos. Sci. Technol.* 67 (2007) 2657–2664, <https://doi.org/10.1016/j.compscitech.2007.03.006>.
- [100] M. Kouzeli, A. Mortensen, Size dependent strengthening in particle reinforced aluminium, *Acta Mater.* 50 (2002) 39–51, [https://doi.org/10.1016/S1359-6454\(01\)00327-5](https://doi.org/10.1016/S1359-6454(01)00327-5).
- [101] R. Arsenault, N. Shi, Dislocation generation due to differences between the coefficients of thermal expansion, *Mater. Sci. Eng.* 81 (1986) 175–187, [https://doi.org/10.1016/0025-5416\(86\)90261-2](https://doi.org/10.1016/0025-5416(86)90261-2).
- [102] Z. Zhang, D. Chen, Consideration of Orowan strengthening effect in particulate-reinforced metal matrix nanocomposites: a model for predicting their yield strength, *Scripta Mater.* 54 (2006) 1321–1326, <https://doi.org/10.1016/j.scriptamat.2005.12.017>.
- [103] R. Aikin, L. Christodoulou, The role of equiaxed particles on the yield stress of composites, *Scripta Metall. Mater.* 25 (1991) 9–14, [https://doi.org/10.1016/0956-716X\(91\)90345-2](https://doi.org/10.1016/0956-716X(91)90345-2).
- [104] J. Luster, M. Thumann, R. Baumann, Mechanical properties of aluminium alloy 6061–Al2O3 composites, *Mater. Sci. Technol.* 9 (1993) 853–862, <https://doi.org/10.1179/mst.1993.9.10.853>.
- [105] E. Hall, The deformation and ageing of mild steel: III discussion of results, *Proc. Phys. Soc. B* 64 (1951) 747–753, <https://doi.org/10.1088/0370-1301/64/9/303>.
- [106] I. Toda-Caraballo, E. Galindo-Nava, P. Rivera-Díaz-del-Castillo, Understanding the factors influencing yield strength on Mg alloys, *Acta Mater.* 75 (2014) 287–296, <https://doi.org/10.1016/j.actamat.2014.04.064>.
- [107] O. Ogurtani, D. Senyildiz, G. Cambaz Buke, Wrinkling of graphene because of the thermal expansion mismatch between graphene and copper, *Surf. Interface Anal.* 50 (2018) 547–551, <https://doi.org/10.1002/sia.6423>.
- [108] B. Han, D. Dunand, Microstructure and mechanical properties of magnesium containing high volume fractions of yttria dispersoids, *Mater. Sci. Eng., A* 277 (2000) 297–304, [https://doi.org/10.1016/S0921-5093\(99\)00074-X](https://doi.org/10.1016/S0921-5093(99)00074-X).
- [109] S. Vlaic, N. Rougemaille, A. Artaud, V. Renard, L. Huder, J.L. Rouvière, A. Kimouche, B. Santos, A. Locatelli, V. Guisnet, Graphene as a mechanically active, deformable two-dimensional surfactant, *J. Phys. Chem. Lett.* 9 (2018) 2523–2531, <https://doi.org/10.1021/acs.jpcclett.8b00586>.
- [110] A. Salem, S. Kalidindi, S. Semiatin, Strain hardening due to deformation twinning in α -titanium: constitutive relations and crystal-plasticity modeling, *Acta Mater.* 53 (2005) 3495–3502, <https://doi.org/10.1016/j.actamat.2005.04.014>.
- [111] P. Hazzledine, P. Hirsch, A coplanar Orowan loops model for dispersion hardening, *Philos. Mag.* 30 (1974) 1331–1351, <https://doi.org/10.1080/14786437408207286>.
- [112] D. Qian, W. Liu, R. Ruoff, Load transfer mechanism in carbon nanotube ropes, *Compos. Sci. Technol.* 63 (2003) 1561–1569, [https://doi.org/10.1016/S0266-3538\(03\)00064-2](https://doi.org/10.1016/S0266-3538(03)00064-2).
- [113] D. Hull, T. Clyne, *Basic Composite Mechanics, an Introduction to Composite Materials*, second ed., Cambridge University Press, Cambridge, New York, 1996, pp. 12–41.